Title: Formation mechanism of porous reaction-bonded silicon nitride with interconnected pores in the presence of MgO

Authors: Raheleh Nikonam M., Martin D. Pugh, Robin A.L. Drew

PII: S0955-2219(18)30663-0
DOI: https://doi.org/10.1016/j.jeurceramsoc.2018.10.032
Reference: JECS 12150

To appear in: *Journal of the European Ceramic Society*

Received date: 11 October 2018
Accepted date: 31 October 2018

Please cite this article as: Nikonam M. R, Pugh MD, Drew RAL, Formation mechanism of porous reaction-bonded silicon nitride with interconnected pores in the presence of MgO, *Journal of the European Ceramic Society* (2018), https://doi.org/10.1016/j.jeurceramsoc.2018.10.032

Formation mechanism of porous reaction-bonded silicon nitride with interconnected pores in the presence of MgO

Raheleh Nikonam M. [a,] *, Martin D. Pugh [a], Robin A. L. Drew [a]

[a] Department of Mechanical, Industrial and Aerospace Engineering, Concordia University, Montreal, CANADA, H3G 1M8

corresponding author: r_nikona@encs.concordia.ca

Abstract

In porous reaction bonded silicon nitride, whiskers normally grow in globular clusters as the dominant morphology and deteriorate the pore interconnectivity. However, the ceramic microstructure was significantly transformed with the addition of MgO; specifically, the morphology was modified to a combination of matte and hexagonal grains. Microstructural observation along with thermodynamic studies suggest that MgO interfered with the presence and nitridation of $SiO_{(g)}$. Consequently, rather than being involved in the whiskers' formation, surface silica instead reacted with volatile MgO to form intermediate products. Through these reactions, whisker formation was blocked, and a porous interconnected structure formed which was confirmed by 3D tomography. After heat-treatment at 1700°C, β-Si_3N_4 crystallized in a glassy matrix containing magnesium. Resulting samples had an open-pore structure with porosity of 74-84 vol. %, and density of 0.48-0.75 g.cm^{-3}. Combination of high porosity and pore size of <40 μm led to compressive strengths of 1.1 to 1.6 MPa.

Key words

Silicon nitride, reaction mechanism, whiskers, magnesium oxide, pore morphology

1. Introduction

According to Gibson and Ashby, porous structures represent a class of materials where a continuous network of the solid skeleton forms the edges and faces of pores. Exhibiting a special combination of high surface area, low density, low specific heat and high thermal insulation makes them widely applicable in various industrial fields [1, 2]. As porous structures can be quite complex, both application and performance of these materials are determined by the characteristics of their pores, i.e. texture, size, distribution and interconnectivity. For applications in tissue engineering scaffolds, environmental filters, forced convection heat-exchangers for electronics devices and aerospace fluid storage tanks, open pores are favored which make the structure permeable. Channel interconnectivity is the key factor allowing the uninterrupted flow of fluid through a membrane. In addition, at a constant porosity, both permeability and flow rate of a porous media are controlled by channel diameter. To target the applications where transport of high temperature fluids is required, the possibility of being able to design the porous ceramic structure is crucial [3-9].

By offering excellent thermal shock resistance and mechano-chemical stability, the high temperature capability of porous silicon nitride (Si_3N_4) to 1700˚C makes this ceramic an attractive candidate for molten metal and exhaust particulate filters [10]. In production of cellular Si_3N_4, there have been several successful manufacturing techniques, e.g. aqueous gel-casting [11], spray-dried method [12], protein foaming [13], sacrificial template [7, 14], emulsions, and replication of polymer foams [2]. However, the significant disadvantages of these processes are high cost of the starting silicon nitride powder and difficulty with machining of the final components which have limited their widespread usage. By maintaining the original dimensions, reaction bonding of silicon nitride (RBSN) is an easy and economical process that enables fabrication of complex shapes with low shrinkage of ±0.1 % and inherent porosity of ~20 % [7, 10, 15]. In this method, elemental silicon of any physical condition can react with nitrogen in the temperature range of 1250˚C to 1450˚C. Additionally, the silicon dioxide layer, which naturally exists on the surface of silicon, will contribute to the nitriding reaction by generating silicon monoxide gas. As an interesting feature, the nature of the nitriding reaction can alter the grain growth, crystallographic structure (α or β), and the resultant morphology of the RBSN grains, i.e., matte, hexagonal or whisker [5, 15-18].

As a reinforcing material for ceramic, glass or metal matrix composites, silicon nitride whiskers have received wide attention, mostly because of their high specific modulus, high specific strength, fracture toughness, and enhanced wear resistance. Having the advantage of better mechanical performance, the fracture toughness of whisker-reinforced composites depend on the whisker characteristics, i.e., radius, length, strength and elastic modulus [19-21]. However, whisker agglomerates often cause an inhomogeneous structure and hinder further improvement of fracture toughness and mechanical properties [22]. In addition to the toughening potential of whiskers, simultaneously they affect the pore characteristics in a porous structure.

Homogenously dispersed SiC whiskers in a porous alumina substrate can enhance the filtering efficiency of particles by hindering their flow and by providing a large specific surface area as an absorption site [23]. However, as permeability is related to the open porosity and pore size, whiskers grow into void spaces and as the pore size decreases, the permeability reduces continuously [24-27].

In the production of highly porous RBSN structures, pore-forming agents, e.g. polymer beads were employed as sacrificial templates [7, 10, 28, 29]. Using this method, despite a homogenous distribution of pores and a controllable range of porosity, the production of a highly porous structure with a designed pore shape has been a challenge as the high free surface area leads to the formation of whisker agglomerates occupying the precursor cavities. While struts were composed of matte and hexagonal grains, whisker clusters grow within the pores, and thus, a suitably permeable porous body could not be obtained [29]. Therefore, a well understood mechanism is required to be able to control the formation of whiskers during the in situ nitridation of silicon.

The α structure of silicon nitride, which is thermodynamically unstable, forms equiaxed matte grain, whereas β-hexagonal exhibits elongated stable grains. Many studies have determined that through reaction with surface silica at temperatures between 1700˚C to 1900˚C, oxide additives promote the α- to β-Si_3N_4 phase transformation by nucleation and grain growth in the solution-precipitation stage of liquid-phase sintering (LPS). In combination with various oxides such as La_2O_3, Y_2O_3 and Yb_2O_3, MgO has been typically used as a Si_3N_4 sintering aid with the main function of densification. Given the favorable integration of the LPS process and inexpensive nitriding reaction, it has been of special interest to study post-sintered RBSN ceramics and the influence of sintering aids on the nitriding behavior of silicon particles. With various melting points and viscosities of eutectic melts, therefore, different microstructures of post-sintered bodies are expected. In addition, as these additives may be included in the starting silicon before nitriding, an effect on the nitridation behavior and thus phase

transformation, reaction rate and grain morphology is very likely [5, 10, 15, 30]. For instance, compared to the Al_2O_3-Y_2O_3 system, MgO-Y_2O_3 additions have been shown to increase the relative density, α/α+β phase ratio and percent nitridation of the post-sintered bodies [25]. Grain morphology and whisker formation in RBSN ceramics have also been affected by adding MgO, unlike Al_2O_3-Y_2O_3 additions [31]. Most of these investigations, however, were carried out on low porosity samples, and studies focused on the interaction of these additives on the nitriding reaction are quite limited [5, 10, 31]. Besides, no detailed information is available concerning the influence of MgO on the mechanism of grain morphology modification.

To achieve a more precise control over the pore shape and interconnectivity of channels in porous RBSN, the objective of the current research was to study the nitriding reaction mechanism, crystallization and pore morphology modification in the presence of MgO. Using sequential nitriding, the migration of elements, phase formation, and reaction mechanism were clarified and then substantiated using available thermodynamic data obtained from FactSage package software. The resultant ceramic composition and microstructure were characterized via XRD, SEM-EDX and 3D tomography analysis. Subsequently, the porosity, density, linear shrinkage, weight loss and compressive strength of the porous bodies were measured as a function of oxide content.

2. Experimental procedure

2.1. Sample preparation

The fabrication method used in this study was based on a published work where the reaction-bonding process has been combined with gel casting and a sacrificial template using polymer microbeads [29]. A uniform slurry was formed by dispersing silicon powder (99.995 %, 8 microns, ABCR) and PMMA beads (Microbeads, 10-40 μm) in deionized water with the weight ratio of Si: PMMA: H_2O of 16: 44: 40. Various contents of MgO powder (>99 % purity, -325 mesh, Sigma-Aldrich) up to 12 wt. % of the resulting Si_3N_4 were then added. Using a monomer, cross-linker and gel-casting rheological agents, a uniform slurry was achieved at pH of 8.5, which was then cast and heated to complete the polymerization step. The porous silicon structure was created by polymer burn-out at 525˚C for 2 h of the de-molded dried bar. To produce porous RBSN, nitriding was carried out in a high purity nitrogen atmosphere (99.999 % purity, O_2 <2 ppm, H_2O <3 ppm, THC <0.5 ppm). Microstructural changes and phase transformation of samples during the nitriding process were investigated with a sequential heating process up to 1425˚C. The dwell time at this temperature was 4 h, whereas at lower temperatures samples were heated for 10 min. A further heat-treatment step at 1700˚C for 2 h was

then performed by immersing samples in a powder bed comprising Si_3N_4, BN and MgO powder. The latter minimized thermal decomposition of the ceramic body and loss of MgO by creating a local gas equilibrium.

2.2. Characterization of the samples

To determine the phase transformation during heat-treatment, X-ray diffractometry (XRD; X'Pert Pro, Panalytical) was carried out using CuKα radiation on the crushed samples. Identification of phases was achieved by comparing the diffraction pattern of the samples with JCPDS standard cards. According to the equation by Gazzara and Messier, the percentage of α- and β-Si_3N_4 can be evaluated by comparing the diffraction intensities of (101) and (210) reflections for the β-phase, and (102) and (201) reflections for α-phase [32].

Scanning electron microscopy (SEM, Hitachi, S-3400 N) was used to study the morphology and interconnectivity of the porous structure. Au-coated fracture surfaces of samples were studied under high vacuum with 5-15 kV and 40-50 mA imaging conditions. X-ray micro-tomography (SkyScan 1172, camera pixel of 3 μm) was performed on a $3\times3\times12$ mm^3 sintered sample to obtain a three-dimensional image of the porous body.

In addition to the conventional SEM imaging, EDX mapping and point analysis (Oxford Instruments, Wave Model) were performed to identify elements and detect their distributions on the polished surface. For this, a low viscosity, slow-curing epoxy resin was used to infiltrate the pore volume inside a vacuum chamber. The surface of the sample was then ground and polished with different diamond pastes down to 0.5 μm for microscopic observation.

Using Archimedes' technique, ASTM C373-88 standard, the density and porosity of samples were measured. Linear shrinkage and weight loss were calculated for eight identically processed samples. Cylindrical samples with the aspect ratio of ~1.3 (height of 15 mm and diameter of 11 mm) were subjected to uniaxial compression testing using an Instron-3382 machine. Data were recorded at 0.4 sec intervals during testing with a pre-test crosshead velocity of 0.5 $mm.sec^{-1}$ and a test crosshead velocity of 0.5 $mm.min^{-1}$. The strengths presented are the average values of five individual tests.

3. Results and Discussion

3.1. Nitridation process

Prior to the nitriding reaction, the dried bodies were heated to 525˚C for 2 h in order to burn-out the polymer beads and reveal a porous silicon structure. SEM micrographs of fracture surfaces of dried and pyrolysed samples are shown in **Fig. 1**. Polymer burn-out during the pyrolysis step led to the formation of a porous structure with uniform pore distribution. With **Fig. 1-b** originating from the uniform structure of the dried body, **Fig. 1-a** microstructure indicates that the PMMA beads did not aggregate during suspension preparation. SEM observation revealed that the porous structure of the pyrolysed samples with and without MgO were essentially the same at this stage. Spherical pores connected with one another through more or less semi-circular windows on the strut's walls created a 3D interconnected structure. Pore size distribution in this sample was a function of the polymer particle size, i.e., 10, 20 and 40 μm; however, due to the pyrolysis linear shrinkage, a slight shift to smaller values are generally expected.

Fig.1. SEM micrographs of a) as dried precursor containing polymer beads and b) after pyrolysis

3.1.1. Whiskers formation in the absence of MgO

Grain morphologies of the nitrided samples with no additive are presented in **Fig. 2**. Along with formation of whiskers as the dominant morphology, some matte and hexagonal grains were observed in minor amounts. The α-matte deposits as small grains when Si vapor reacts with nitrogen through a gaseous phase reaction and continues by evaporation-condensation or diffusion of Si atoms to the nucleation sites. In contrast, the elongated β-Si_3N_4 hexagonal grains mainly grow when nitrogen diffuses in liquid or solid Si [15]. **Fig 2-a,** and **-b** revealed that silicon nitride whiskers were randomly elongated in different directions and formed spherical clusters occupying pore cavities. Most of these grains were quite straight, short and polyhedral in cross-section, which suggests they are potentially β-silicon nitride [33]. Some of them were characterized by the presence of small beads on their tips that were found to contain Si (61 wt. %), N (33 wt. %) and O (6 wt.%), based on EDX microanalysis. This was evidence that silicon nitride whisker growth proceeded through a vapor-liquid-solid (VLS) mechanism: where nitrogen and silicon monoxide gas species dissolve in a liquid droplet. The chemical composition of the starting silicon powder listed in **Table 1** revealed the presence of impurities, which usually form low viscosity melts, especially compounds of iron and aluminum. The presence of these beads on growing whiskers suggests that the growth process was probably incomplete, and the whiskers would have grown further given more time at temperature [15, 34, 35].

Fig. 2. SEM of fracture surface at two different magnifications illustrating the blocked pores with silicon nitride whiskers

Table 1. Chemical compositions of the starting silicon

An oxygen impurity of 1.3 wt. % in the starting silicon (**Table 1**) can be assumed to be mostly in the form of native surface silica. In the Si-O system, the stability region of different silicon oxides is a function of temperature and oxygen partial pressure in the ambient atmosphere, so by decreasing pO_2/p^{θ} at high temperature, SiO_2 becomes unstable and SiO vapor is generated [36]. In this regard, despite the positive ΔG° of **Eq. 1,** at high temperature and an oxygen partial pressure below the critical amount, reduction of surface silica on silicon becomes feasible. Considering that nitriding occurred under an atmosphere of 99.999 % purity nitrogen gas, the pO_2 would have been lower than 10^{-5} atm. This low oxygen content could enhance the partial pressure of SiO at the oxide-silicon interface and supply volatile SiO gaseous species for the formation of silicon nitride whiskers according to **Eq. 2** [10, 34, 36]. With the evaporation rate of 10^{-6} kg.m^{-2}.sec^{-1}, the vapor pressure of silicon would be of the order of 10^{-7} atm at 1350˚C [16]. Furthermore, considering that a high degree of porosity should promote silicon vaporization, the oxygen generated from the nitriding reaction zone would lead to the active oxidation of silicon, and thus, an increased partial pressure of SiO species via **Eq. 3**. Accordingly, the re-oxidation cycle accelerated whisker formation, which blocked the open pore volume. As nitriding through the gaseous phase reaction between SiO and N_2 proceeds at a much faster rate than that involving Si vapor, correspondingly whisker formation occurs prior to the formation of matte or hexagonal grains [15, 16, 36]. ΔG° of reactions were calculated using the "Reaction" module in FactSage 6.4 package software.

$SiO_2\ (g) + Si\ (s) \leftrightarrow 2SiO\ (g)$, **Eq. 1**

$\Delta G^{\circ} = -328.1\times10^{-3}T+595.4$ kJ.mol^{-1} (867~1412˚C)

$\Delta G^{\circ} = -292.8\times10^{-3}T+545.9$ kJ.mol^{-1} (1412~1465˚C)

$3\ SiO\ (g) + 2\ N_2\ (g) \leftrightarrow Si_3N_4(s) + 3/2\ O_2$ **Eq. 2**

$\Delta G^{\circ} = 619.8\times10^{-3}T-354.7$ kJ.mol^{-1}

$Si(g) + 0.5O_2(g) \leftrightarrow SiO(g)$ **Eq. 3**

$\Delta G^{\circ} = -82.4\times10^{-3}T-125.1$ kJ.mol^{-1} (25~1412˚C)

3.1.2. Morphology modification in the presence of MgO

With the dominant microstructure of matte and hexagonal grains, SEM images in **Fig. 3** show that the addition of MgO in the starting silicon significantly reduced whisker formation. It seems that the open pore structure in **Fig. 3-a** and **-c** allows whiskers to become more elongated compared to **Fig. 2-a,** where the available space for grain growth was more constrained and the length of whiskers is

observed to be shorter. By increasing the amount of MgO to 9 wt. %, gradually the magnitude of whisker formation decreased. At 12 wt. % MgO, almost no whiskers were evident, and all the silicon nitride was either in the form of matte or hexagonal grains. With significant MgO present (**Fig. 3-g**) the pore morphology and characteristics were completely different compared to no additive, **Fig. 3-h**. The pores became regular and spherical with diameters less than 40 μm instead of irregularly shaped whisker-blocked pores. The open versus blocked-pore morphology is even more obvious on their polished cross-sections shown in **Fig. 4**. Based on the contrast between dark regions (resin) and light regions (ceramic), pore cavities, whiskers and solid struts can be distinguished. For the same nitriding time, the unfilled cavities in the sample with no additive show the whisker-blocked pore structure, diminishing the structure's permeability. Whereas with 12 wt. % MgO, the pore structure appears entirely whisker-free and interconnected which allowed the resin to completely infiltrate the microstructure and fill the cavities.

Fig. 3. SEM of fracture surfaces illustrating the pore structures in the presence of different MgO contents nitrided at 1425ºC; a and b) 3 % MgO, c) 6 % MgO, d) 9 % MgO, and e, f and g) 12 % MgO, and compared to h) 0 % MgO

Fig. 4. Polished resin-infiltrated cross-sections showing the pore structures in silicon nitride containing a) 0 % MgO and b) 12 % MgO

Fig. 5 and **Table 2** show, respectively, the XRD patterns and relative phase ratios of the nitrided samples with different contents of MgO. After heating for 4 h, nitridation was complete as no residual silicon was detected in the nitrided samples. N_2 gas could easily have diffused into the interior region of the porous Si body through the permeable pore channels. In such an open porous network the nitriding reaction proceeds very quickly compared to conventional RBSN structures with low porosity, which can take several days of heating for full nitridation depending on component size [15].

Table 2 shows that, along with both the α and β polymorphs of Si_3N_4, minor amounts of silicon oxynitride (Si_2N_2O) formed when MgO was added. The α-Si_3N_4 content was higher in all MgO-containing samples compared to those comprising no MgO and indicates preferential formation of the α-phase. Considering that in the MgO-SiO_2 system the first eutectic liquid forms at a somewhat higher temperature (1543-1557˚C) than the nitriding temperature, we can assume that the α/β-phase ratio was not due to liquid formation. While the less stable α-phase is known to dissolve oxygen, β-silicon nitride contains no oxygen [15, 16]. Therefore, an increased presence of oxygen in the system

originating from the oxide additive promoted the preferential formation of α-phase. To define the role of this oxide in the microstructural changes of the porous RBSN, samples contain 12 wt. % MgO were sequentially heated up to a temperature of 1700˚C.

Fig. 5. XRD patterns of material nitrided at 1425ºC with 0, 3, 6, 9 and 12 % MgO (α, β and ∗ show peaks corresponding to α-Si_3N_4, β-Si_3N_4 and Si_2N_2O, respectively)

Table 2. Phase fractions and α/β-Si_3N_4 phase ratio obtained by XRD from samples containing different MgO contents and nitrided at 1425ºC

The XRD results and phase compositions presented in **Fig. 6** and **Table 3** revealed that Si and MgO were the only crystalline phases detected in the sample after the pyrolysis step. By heating the porous silicon body to 1100˚C, some minor peaks between 2θ of 20˚ to 45˚ were present which corresponded to ~3 wt. % Forsterite, Mg_2SiO_4 as well as residual MgO.

Fig. 6. XRD patterns of samples containing 12 % MgO heat-treated at 525, 1100, 1200, 1300, 1350, 1400, 1425 and 1700℃(α, β , ∗, ∨, × and ■ show peaks corresponded to α-Si_3N_4, β-Si_3N_4, Si_2N_2O, Mg_2SiO_4, MgO and Si, respectively)

Table 3. Phase fractions and α/β-Si_3N_4 phase ratio obtained for samples containing 12 % MgO and heat-treated at different temperatures

At 1200˚C, while the Mg_2SiO_4 peaks intensified up to a maximum of ~9 wt. % content, crystalline MgO was no longer detected. Experimentally Mg_2SiO_4 can be formed at temperatures between 1000˚C and 1400˚C by reaction between solid or gaseous MgO (g,s) and native surface SiO_2 present on the surface of silicon particles [37]. Thermodynamic data in **Eq. 4** confirms that this reaction can involve either gaseous or solid MgO, both of which have large negative ΔG˚. However, with MgO vapor present, the reaction is much more thermodynamically favorable. In an experiment where porous silicon (without additive) was placed on MgO powder during nitridation, it is revealed in **Fig. 7** that the formation of whiskers was stopped. Indeed, a similar microstructure is observed in **Fig. 3-g** (12 % MgO addition), in which the pore cavities became entirely spherical and whisker-free. This both confirms that MgO is highly volatile at elevated temperature and also that it interfered with the nitriding reaction to change the microstructure and morphology of the porous Si_3N_4.

$2MgO\,(g, s) + SiO_2\,(s) \rightarrow Mg_2SiO_4\,(s)$ **Eq. 4**

$\Delta G_g^{\circ} = 368.9\times10^{-3}\ T - 10^{+3}\ kJ.mol^{-1}$ (866~1465˚C)

$\Delta G_s^\circ = 62.4\times10^{-3}\ T - 100.5\ kJ.mol^{-1}$ (800~1465˚C)

Fig. 7. SEM micrograph of pure silicon precursor nitrided on top of MgO powder bed

In addition, a relatively uniform elemental distribution of Mg and O around the Si particles shown in **Fig. 8** suggests that magnesium silicate formed predominantly through reaction of an Mg-containing gaseous phase rather than that of a solid phase. Aside from the elevated temperature, the high surface area and levels of porosity would enhance the vaporization rate. Accordingly, Mg-containing vapor migrated to the silica-rich surface and reacted to form Mg_2SiO_4 [38-40]. The protective SiO_2 layer acting as a "sink" for magnesium, reacted with gaseous magnesium oxide rather than with the silicon and hence SiO gas formation was suppressed. It is worth noting that under neutral and reducing atmospheres, along with molecular MgO, the major vapor species in thermodynamic equilibrium with solid MgO are reported to be O_2 (g) and Mg (g) [41]. Therefore, we can expect that with vaporization of MgO, the local oxygen vapor pressure in the pore volume would increase and alter the partial pressure of the SiO in the very early stage of nitriding. This is also in agreement with the higher α-Si_3N_4 content in samples containing MgO compared to that of silicon nitride with 0 % MgO (**Table 1**) since small amounts of oxygen to the reaction zone are reported to alter the α/β-Si_3N_4 ratio [42].

Fig. 8. EDX mapping of 12 % MgO addition to the porous silicon precursor and nitrided at different temperatures (note Mg and O segregation on the particle surfaces)

The XRD pattern of samples with 12 % MgO additions showed the formation of both α- and β- Si_3N_4 at 1350˚C with α being the dominant phase. As the temperature was increased to 1425˚C, the α/β ratio decreased and is attributed to the melting of silicon and formation of more β phase. After 4 h heating, Si_2N_2O coexisted along with silicon nitride up to an amount of ~15 wt. %. Unfortunately, due to the similar elemental contrast of these two phases and the limited resolution of the EDX system, microstructural distinction between Si_3N_4 and Si_2N_2O phases was not possible.

Formation of Si_2N_2O has been reported at temperatures ≥1700˚C due to oxidation of Si_3N_4 [43-46]. In the current work, Si_2N_2O formed at a lower temperature, just prior to any silicon nitride formation and confirmed that oxidation of Si_3N_4 was not involved in the development of this phase. On the other hand, the appearance of Si_2N_2O coincided with a simultaneous decrease in magnesium silicate content when MgO was present. Therefore, by decomposition of Mg_2SiO_4, as an intermediate phase through reaction with nitrogen, formation of Si_2N_2O was initiated and enhanced by the presence of oxygen. The calculated Gibbs free energy for this reaction described in **Eq. 5** gives a very large negative ΔG˚,

indicating that this reaction is very thermodynamically favorable. Further formation of Si_2N_2O could have occurred through oxidation of silicon due to the increased local pO_2 [36].

$Mg_2SiO_4(s)+3Si(s)+2N_2(g)\rightarrow 2Si_2N_2O(s)+ 2MgO\ (s, g)$ **Eq. 5**

$\Delta G^{\circ} = 371.8T - 745\times10^{+3}\ kJ.mol^{-1}$ (640~1414˚C)

Based on these observations, in the presence of MgO, a decrease in whisker formation was found to coincide with an increase in Mg_2SiO_4 and Si_2N_2O contents. This favored the formation of equiaxed grains of Si_3N_4 rather than whiskers. Given the fact that the Si_3N_4 morphology is closely related to the gaseous partial pressure of the various species present, MgO changed the partial pressure of the reactants, thus modifying the grain morphology to a mixture of matte and hexagonal grains. Consequently this created an open and interconnected porous microstructure.

3.2. High Temperature Heat-treatment

3.2.1. Effect on Microstructure

When MgO-containing nitrided samples were further heated to 1700ºC for 2 h, the only detectable crystalline phase was β-Si_3N_4. Consequently, it is proposed that silicon oxynitride, remaining after nitriding, contributed to liquid phase formation and enabled complete α- to β-Si_3N_4 phase transformation. **Fig. 9** presents the overall microstructural evolution during heat-treatment from the silicon precursor shown in **Fig. 9-a**, to the final β-Si_3N_4 microstructure in **Fig. 9-d**. It is clear from **Fig. 9-b** that the nitriding reaction initiated at the surface of the Si and progressed inwards by diffusion of nitrogen. Once a nitride layer covered the surface of the silicon particles, further nitridation depended on the diffusion of nitrogen through the surface silicon nitride layer [15]. Fully nitrided grains, observed in **Fig. 9-c,** were a combination of α- and β-phase. The elongated β-Si_3N_4 grains in **Fig. 9-d** developed during liquid phase transformation. XRD pattern of the sample in **Fig. 6** confirmed that the only phase present in this structure was β-Si_3N_4.

Fig. 9. Microstructural development and grain growth of the Si precursor containing 12 % MgO after heat-treatment at different temperatures: a) 1100℃, b) 1400℃, c) 1425℃ and d) 1700℃

SEM micrographs of MgO-containing samples in **Fig. 10** shows that after heat-treatment at 1700ºC, the β phase precipitated as elongated hexagonal grains. In samples containing 3 % MgO, local supersaturation led to abnormal grain growth in abundant regions of liquid phase. Low content of sintering additives resulted in the formation of grains with various sizes and thus, an inhomogeneous microstructure, as shown in **Fig. 10-a** and **-b**. By increasing the MgO content and Si_2N_2O phase ratio,

the amount of liquid phase became high enough that the low viscosity melt migrated to the boundaries and suppressed the abnormal grain growth. Hence, with homogenous distribution of liquid phase during the heat-treatment process, grain growth occurred in multiple regions and fine β-Si_3N_4 with uniform size distribution were precipitated in the 6 % MgO samples. From 9 wt. % to 12 wt. % MgO, while the length of the rod-like grains remained relatively constant indicating negligible grain growth on the β-basal plane (001), grain coarsening occurred mainly on the prismatic planes (100). Grains with the maximum length of 6 μm were surrounded by glassy phase as indicated by arrows in **Fig. 10-g**. The results of EDX analysis of this figure showed the presence of magnesium, nitrogen and oxygen in the form of an M-Si-O-N oxynitride amorphous phase.

X-ray micro-tomography was used as a non-destructive analysis to visualize and characterize the porosity of the heat-treated structure. Through the LPS process, all whiskers vanished, and the precipitated hexagonal β-grains formed the struts in the resulting porous microstructure.

The interconnected pore network of 12 wt. % MgO samples was observed in 2D cross-sections of eight sequential slices cut through z axis (**Fig. 11**). Furthermore, 3D construction images of thin layers with a thickness of 116 μm, illustrate a continuous network of pore channels interconnected in three-dimensional space (**Fig. 12**). The pores were relatively uniform and completely whisker-free; consequently, a porous structure with high interconnectivity was obtained.

Fig. 10. SEM micrographs of various MgO precursor contents heat-treated at 1700°C: a and b) 3 % MgO, c and d) 6 % MgO, e) 9 % MgO, f) 12 % MgO and g) shows glassy phase and EDX spectrum of (f)

Fig. 11. Slice images of xyz planes for eight sequential slices of porous silicon nitride containing 12 % MgO (green region shows the solid body and black areas are pores)

Fig. 12. 3D reconstruction images of porous silicon nitride ceramic (orange region shows the solid body)

3.2.2. Properties of the porous samples

The weight losses and linear shrinkages obtained as a function of additive content are plotted in **Fig. 13.** Thermal decomposition of Si_3N_4 and evaporation of MgO were the main sources of weight loss which can be controlled by the contents of liquid phase and partial pressure of MgO in the ambient atmosphere. Therefore, from 0 to 9 % MgO, weight loss was increased as liquid phase formation was enhanced with higher additive contents. However, the sudden drop at 12 wt. % MgO is explained by

the high partial pressure of volatile MgO diffusing from the powder bed, which could be high enough in the local atmosphere to effectively suppress oxide loss.

The smallest shrinkage (0.4 %) was found with 3 % MgO content, whereas the highest shrinkage (1.6 %) occurred in the case of 12 % MgO owing to the presence of more liquid phase. Particle size and shape, type and amount of oxide additives are the main factors governing the shrinkage and densification behavior during heat-treatment at this temperature. In typical LPS, if the amount of low viscosity liquid phase is high enough, the liquid penetrates between the grains and induces the first stage of shrinkage by grain rearrangement. Later, through solution-precipitation and densification, further shrinkage is observed. In post-sintering of RBSN, however, the particle rearrangement would not occur as bonding between nitrided grains hinder the effect of capillary forces. This leads to the low shrinkage of all samples indicating that the dimensions of the nitrided bodies remained virtually unchanged during heat-treatment at 1700°C. By increasing the oxygen content of the system, originating from MgO, silica or Si_2N_2O, accumulation of liquid phase could result in some particle rearrangement and enhanced shrinkage through solution of α-phase and neck junctions [5, 15]. The overall LPS shrinkage results in a decrease in porosity and thus some densification. **Fig. 14** shows the bulk density and apparent porosity for 12 % MgO samples heat-treated at 1700°C is ~74 vol. % and 0.75 $g.cm^{-3}$ compared to ~81 vol. % porosity and 0.53 $g.cm^{-3}$ density for as-nitrided samples. Therefore, the post-nitriding heat-treatment step in the presence of MgO led to the some densification and a slight decrease in porosity. However, for lower MgO contents a different trend was observed: for 6 % MgO addition, the porosity was ~84 vol. %, and the bulk density decreased to ~0.48 $g.cm^{-3}$ and is attributed to MgO evaporation. However, at higher MgO content, lower porosity and a denser structure was achieved due to the densification promoted by liquid phase formation.

3.2.3. Compression Testing

Compression tests were carried out on samples heat-treated at 1700°C and the results are presented as a function of oxide content in **Fig. 15**. As strength is closely related to microstructure, the high porosity content of samples led to the relatively low compressive strengths. Low-magnification SEM micrographs of samples contain 6 and 12 wt. % MgO show the differences in their cellular structures. The highest porosity content, 6 % MgO, showed a compressive strength of ~1.1 MPa whereas with enhanced shrinkage and a lower porosity of 74 vol. %, the 12 % MgO samples led to a higher strength of ~1.6 MPa. These values are comparable with those reported for cellular Si_3N_4 structures fabricated for biomedical applications [6]. In the latter case, interconnected large pores and high porosity are

considered suitable for tissue in-growth and nutrition delivery [6]. The compression testing data are in good agreement with the microstructures of samples; therefore, we can assume that in the current study, the high porosity content was the main factor limiting the compressive strength. In addition to the influence of porosity, one should consider the differences in pore size distribution of samples, especially the fact that pores are major flaws in any porous structure and the maximum and mean pore size highly affect the mechanical properties of samples. Although the amount and size of polymer beads were essentially the same for all samples; with different MgO content, samples experienced various linear shrinkage; thus, resulting in different pore size distribution.

Fig. 13. Linear shrinkage and weight loss vs MgO content for samples heat-treated at 1700℃

Fig. 14. Porosity and density variation vs MgO content after heat-treatment at 1700℃

Fig. 15. Compressive strength of samples vs MgO content heat-treated at 1700ºC

Conclusion

The formation and morphology change of highly porous RBSN structure was investigated in the presence of MgO. Quantitative and visual comparisons showed a strong correlation between the ceramic's composition and morphology of grains. In the presence of MgO, Mg_2SiO_4 formed as an intermediate phase predominantly via a gaseous phase reaction between MgO and surface silica. At higher temperature, with a concurrent decrease in the content of Mg_2SiO_4, Si_2N_2O formed and coexisted with α-Si_3N_4 at 1425˚C. This mechanism significantly altered the dominant reaction, simultaneously modifies the grains morphology to fine equiaxed grains and enhances the pore channel interconnectivity. From 0 to 12 wt. % MgO, the α/β-phase ratio significantly increased from ~0.4 to ~1.5. Low content of MgO restrained whisker growth and led to the formation of sintered grains with relatively bimodal size distributions. No whiskers appeared with 12 wt. % MgO content during the nitriding process and coarse sintered grains with a uniform size distribution formed in a highly porous interconnected structure. X-Ray tomography confirmed that the pore network extended continuously and homogeneously throughout the microstructure. Upon heat-treatment up to 1700ºC, Si_2N_2O disappeared by its incorporation into a liquid phase out of which β-Si_3N_4 formed. Upon cooling to room temperature, the liquid became a glassy phase and contained magnesium, oxygen and nitrogen. The resulting material showed a high porosity of 74-84 vol. % and density of 0.48-0.75 $g.cm^{-3}$ with a mean compression strength of between 1.1 to 1.6 MPa, with the highest porosity displaying the weakest strengths.

Acknowledgement

The authors wish to acknowledge the support of Natural Sciences and Engineering Research Council of Canada through the Discovery Grants program. R. Nikonam was also supported by internal scholarships from Concordia University. Lastly, we would like to thank Dr. Elmira Moosavi-Khoonsari for her assistance with the thermodynamic calculations.

References

[1] L. J. Gibson and M. F. Ashby, Cellular solids, structure and properties, second ed., University of Cambridge, 1997.
https://doi.org/10.1017/CBO9781139878326

[2] E. Guzi de Moraes, D. Li, P. Colombo and Z. Shen, Silicon nitride foams from emulsions sintered by rapid intense thermal radiation, J. Eur. Ceram. Soc. 35 (2015) 3263–3272.
https://doi.org/10.1016/j.jeurceramsoc.2015.02.007

[3] K. Yamamoto and T. Sakai, Effect of pore structure on soot deposition in diesel particulate filter, Comput. 4 (2016) 1-11.
https://doi.org/10.3390/computation4040046

[4] I. Sabree, J. E. Gough and B. Derby, Mechanical properties of porous ceramic scaffolds: Influence of internal dimensions, Ceram. Int. 41 (2015) 8425-8432.
https://doi.org/10.1016/j.ceramint.2015.03.044

[5] D. Yao, Y. Xia, K.-H. Zuo, D. Jiang, J. Gunster, Y.-P. Zeng and J. G. Heinrich, The effect of fabrication parameters on the mechanical properties of sintered reaction bonded porous Si_3N_4 ceramics, J. Eur. Ceram. Soc. 34 (2014) 3461-3467.
https://doi.org/10.1016/j.jeurceramsoc.2014.06.018

[6] K. Bodisova, M. Kasiarova, M. Domanicka, M. Hnatko, Z. Lences, Z. Varchulova Novakova, J. Vojtassak, S. Gromosova and P. Sajgalik, Porous silicon nitride ceramics designed for bone substitute applications, Ceram. Int. 39 (2013) 8355-8362.
https://doi.org/10.1016/j.ceramint.2013.04.015

[7] Y.-J. Park and H.-D. Kim, Permeability enhancement in porous-sintered reaction-bonded silicon nitrides, Int. J. Appl. Ceram. Tec. 8 (2011) 809-814.
https://doi.org/10.1111/j.1744-7402.2010.02511.x

[8] A. Jena and K. Gupta, Pore structure characterization of ceramic hot gas fiters, Ceram. Eng. Sci. Proc. 22 (2008) 1-8.

https://doi.org/10.1002/9780470294703.ch33

[9] J.-F. Despois and A. Mortensen, Permeability of open-pore microcellular materials, Acta Mater. 53 (2005) 1381-1388.
https://doi.org/10.1016/j.actamat.2004.11.031

[10] D.-V. Tuyen, Y.-J. Park, H.-D. Kim and B.-T. Lee, Formation of rod-like Si_3N_4 grains in porous SRBSN bodies using $6Y_2O_3$-2MgO sintering additives, Ceram. Int. 35 (2009) 2305-2310.
https://doi.org/10.1016/j.ceramint.2009.01.010

[11] T. Wan, D. Yao, J. Yin, Y. Xia, K. Zuo and Y. Zeng, The microstructure and mechanical properties of porous silicon nitride ceramics prepared via novel aqueous gelcasting, Int. J. Appl. Ceram. Tec. 12 (2015) 1-11.
https://doi.org/10.1111/ijac.12424

[12] J. Zhou, J.-p. Fan, G.-l. Sun, J.-y. Zhang, X.-m. Liu, D.-h. Zhang and H.-j. Wang, Preparation and properties of porous silicon nitride ceramics with uniform spherical pores by improved pore-forming agent method, J. Alloy. Comp. 632 (2015) 655-660.
https://doi.org/10.1016/j.jallcom.2015.01.305

[13] L. Yin, X. Zhou, J. Yu and H. Wang, Highly porous silicon nitride foam prepared using a route similar to the making of aerated food, Int. J. Appl. Ceram. Tec. 13 (2015) 395- 404.
https://doi.org/10.1111/ijac.12497

[14] L. Yin, X. Zhou, J. Yu and H. Wang, Preparation of silicon nitride foam with three-dimensional interconnected pore structure, Mater. Design. 89 (2016) 620–625.
https://doi.org/10.1016/j.matdes.2015.10.020

[15] G. Ziegler, J. Heinrich and G. Wotting, Review, Relationships between processing, microstructure and properties of dense and reaction-bonded silicon nitride, J. Mater. Sci. 22 (1987) 3041-3086.
https://doi.org/10.1007/BF01161167

[16] A. J. Moulson, Review, Reaction-bonded silicon nitride: its formation and properties, J. Mater. Sci. 14 (1979) 1017-1051.
https://doi.org/10.1007/BF00561287

[17] L. Han, J. Wang, F. Li and H. Wang, Low-temperature preparation of Si_3N_4 whiskers bonded/reinforced SiC porous ceramics via foam-gelcasting combined with catalytic nitridation, J. Eur. Ceram. Soc. 38 (2018) 1210-1218. https://doi.org/10.1016/j.jeurceramsoc.2017.10.043

[18] L. Li, J.-W. Wang, H. Zhong, L.-Y. Hao, H. Abadikhah, X. Xu, C.-S. Chen and S. Agathopoulos, Novel α-Si_3N_4 planar nanowire superhydrophobic membrane prepared through in-

situ nitridation of silicon for membrane distillation, J. Membr. Sci. 543 (2017) 98-105. https://doi.org/10.1016/j.memsci.2017.08.049

[19] I. C. Jung, S. H. Cho, S. W. Na, J. Lee, H. S. Lee and W. S. Cho, Synthesis of Si_3N_4 whiskers in porous SiC bodies, Mater. Lett. 61 (2007) 4843-4846. https://doi.org/10.1016/j.matlet.2007.03.063

[20] T. Imai, M. Mabuchi, Y. Tozawa and M. Yamada, Superplasticity in β-silicon nitride whisker-reinforced 2124 aluminium composite, J. Mater. Sci. Lett. 9 (1990) 255-257. https://doi.org/10.1007/BF00725816

[21] J. Dusza, P. Sajgalik, Z. Bastl, V. Kavecansky and J. Durisin, Properties of β-silicon nitride whiskers, J. Mater. Sci. Lett. 11 (1992) 208-211. https://doi.org/10.1007/BF00741423

[22] P. Sajgalik and J. Dusza, High-temperature strength and fracture toughness of Si_3N_4-β-Si_3N_4 composites, J. Mater. Sci. Lett. 10 (1991) 776-778. https://doi.org/10.1007/BF00723278

[23] W. S. Park, D. J. Choi and H. D. Kim, Modification of inner pores with silicon carbide whiskers onto the Al_2O_3 substrate by CVI process, Key Eng. Mat. 287 (2005) 212-219. https://doi.org/10.4028/www.scientific.net/KEM.287.212

[24] Yang, Jian-Feng, G.-J. Zhang, N. Kondo and T. Ohji, Synthesis and properties of porous Si_3N_4/SiC nanocomposites by carbothermal reaction between Si_3N_4 and carbon, Acta Mater. 50 (2002) 4831-4840. https://doi.org/10.1016/S1359-6454(02)00350-6

[25] B.-T. Lee and H.-D. Kim, Effect of sintering additives on the nitridation behavior of reaction-bonded silicon nitride, Mater. Sci. Eng. A. 364 (2004) 126-131. https://doi.org/10.1016/j.msea.2003.07.005

[26] Y. Xu, S. Sang, Y. Li, L. L. Y. Zhao and L. Shujing, Pore structure, permeability, and alkali attack resistance of Al_2O_3-C refractories, Metall. Mater. Trans. A. 45 (2014) 2885-2893. https://doi.org/10.1007/s11661-014-2217-1

[27] C. Kawai and A. Yamakawa, Network formation of Si_3N_4 whiskers for the preparation of membrane filters, J. Mater. Sci. Lett. 17 (1998) 873-875. https://doi.org/10.1023/A:1006619413144

[28] L. Yuan, J. Yu and S. Zhang, Effect of pore-forming agent on porous reaction-bonded silicon nitride ceramcis, IOP Conf. Ser.: Mater. Sci. Eng. 18 (2011) 1-4. https://doi.org/10.1088/1757-899X/18/22/222011

[29] A. Alem, M. D. Pugh and R. A. L. Drew, Open-cell reaction bonded silicon nitride foams: Fabrication and characterization, J. Eur. Ceram. Soc. 34 (2014) 599-609. https://doi.org/10.1016/j.jeurceramsoc.2013.09.011

[30] M. Muller, W. Bauer and R. Knitter, Processing of micro-components made of sintered reaction-bonded silicon nitride (SRBSN). Part 1: Factors influencing the reaction-bonding process, Ceram. Int. 35 (2009) 2577-2585. https://doi.org/10.1016/j.ceramint.2009.02.013

[31] A. Alem, R. A. L. Drew and M. D. Pugh, Sintered reaction-bonded silicon nitride foams with a high level of interconnected porosity, J. Mater. Sci. 50 (2015) 570-576. https://doi.org/10.1007/s10853-014-8613-5

[32 C. Gazzara and D. Messier, Determination of phase content of Si_3N_4 by X-ray diffraction analysis, Am. Ceram. Soc. Bull. 56 (1977) 777-780. https://www.scopus.com/inward/record.uri?eid=2-s2.0-0017528898&partnerID=40&md5=53f5c5af80d1bb3c0031258ca935056e

[33] X. Xi, H. Xiong, W. Guo, Q. Jiang, Y. Cheng and H.-T. Lin, Effect of nitrogen pressure on preparation of β-Si_3N_4 whiskers, Ceram. Int. 43 (2017) 10610–10613. https://doi.org/10.1016/j.ceramint.2017.05.038

[34] M.-J. Wang and H. Wada, Synthesis and characterization of silicon nitride whiskers, J. Mater. Sci. 25 (1990) 1690-1698. https://doi.org/10.1007/BF01045372

[35] C. Kawai and A. Yamakawa, Crystal growth of silicon nitride whiskers through a VLS mechanism using SiO_2-Al_2O_3-Y_2O_3 oxides as liquid phase, Ceram. Int. 24 (1998) 135-138. https://doi.org/10.1016/S0272-8842(97)00042-4

[36] G. Yao, Y. Li, P. Jiang, X. Jin, M. Long, H. Qin and R. V. Kumar, Formation mechanisms of Si_3N_4 and Si_2N_2O in silicon powder nitridation, Solid State Sci. 66 (2017) 50-56. https://doi.org/10.1016/j.solidstatesciences.2017.03.002

[37] G. R. Terwilliger and F. F. Lange, Hot-pressing behavious of Si_3N_4, J. Am. Ceram. Soc. 57 (1974) 25-29. https://doi.org/10.1111/j.1151-2916.1974.tb11356.x

[38] G. W. Brindley and R. Hayami, Kinetics and mechanism of formation of forsterite (Mg_2SiO_4) by solid state reaction of MgO and SiO_2, Philos. Mag. 12 (1965) 505-514. https://doi.org/10.1080/14786436508218896

[39] T. Sasamoto, H.-L. Lee and T. Sata, Effects of porosity on vacuum-vaporization of magnesia, J. Ceram. Assoc. 82 (1974) 603-610.
https://doi.org/10.2109/jcersj1950.82.951_603

[40] M. D. Pugh and A. J. Moulson, Vapour transport of magnesia into reaction-bonded silicon nitride, J. Mat. Sci. 30 (1995) 1425-1428.
https://doi.org/10.1007/BF00375242

[41] R. H. Lamoreaux and D. L. Hildenbrand, High-temperature vaporization behavior of oxides ll. Oxides of Be, Mg, Ca, Sr, Ba, B, Al, Ga, In, Ti, Si, Ge, Sn, Pb, Zn, Cd and Hg, J. Phys. Chem. Ref. Data. 16 (1987) 419-443.
https://doi.org/10.1063/1.555799

[42] H. M. Jennings, Review, On reactions between silicon and nitrogen, J. Mater. Sci. 18 (1983) 951-967.
https://doi.org/10.1007/BF00551961

[43] J. L. de la Pena and M. I. Pech-Canul, Microstructure and kinetics of formation of Si_2N_2O and Si_3N_4 into Si porous preforms by chemical vapor infiltration (CVI), Ceram. Int. 33 (2007) 1349–1356.
https://doi.org/10.1016/j.ceramint.2006.05.006

[44] P. Kroll and M. Milko, Theoretical investigation of the solid state reaction of silicon nitride and silicon dioxide forming silicon oxyniride under pressure, Z. Anorg. Allg. Chem. 629 (2003) 1737-1750.
https://doi.org/10.1002/zaac.200300122

[45] B. Bill and H. Heping, The influence of different oxides on the formation of Si_2N_2O from SiO_2 and Si_3N_4, J. Eur. Ceram. Soc. 6 (1990) 3-8.
https://doi.org/10.1016/0955-2219(90)90028-E

[46] Z. K. Huang, P. Greil and G. Petzov, Formation of silicon oxinitride from Si_3N_4 and SiO_2 in the presence of Al_2O_3, Ceram. Int. 10 (1984) 14-17.
https://doi.org/10.1016/0272-8842(84)90017-8

Figure captions

Fig. 1. SEM micrographs of a) as dried precursor containing polymer beads and b) after pyrolysis

Fig. 2. SEM of fracture surface at two different magnifications illustrating the blocked pores with silicon nitride whiskers

Fig. 3. SEM of fracture surfaces illustrating the pore structures in the presence of different MgO contents nitrided at 1425°C; a and b) 3 % MgO, c) 6 % MgO, d) 9 % MgO, and e, f and g) 12 % MgO, and compared to h) 0 % MgO

Fig. 4. Polished resin-infiltrated cross-sections showing the pore structures in silicon nitride containing a) 0 % MgO and b) 12 % MgO

Fig. 5. XRD patterns of material nitrided at 1425°C with 0, 3, 6, 9 and 12 % MgO (α, β and ∗ show peaks corresponding to α-Si_3N_4, β-Si_3N_4 and Si_2N_2O, respectively)

Fig. 6. XRD patterns of samples containing 12 % MgO heat-treated at 525, 1100, 1200, 1300, 1350, 1400, 1425 and 1700°C (α, β , ∗, ∨, × and ■ show peaks corresponded to α-Si_3N_4, β-Si_3N_4, Si_2N_2O, Mg_2SiO_4, MgO and Si, respectively)

Fig. 7. SEM micrograph of pure silicon precursor nitrided on top of MgO powder bed

Fig. 8. EDX mapping of 12 % MgO addition to the porous silicon precursor and nitrided at different temperatures (note Mg and O segregation on the particle surfaces)

Fig. 9. Microstructural development and grain growth of the Si precursor containing 12 % MgO after heat-treatment at different temperatures: a) 1100°C, b) 1400°C, c) 1425°C and d) 1700°C

Fig. 10. SEM micrographs of various MgO precursor contents heat-treated at 1700°C: a and b) 3 % MgO, c and d) 6 % MgO, e) 9 % MgO, f) 12 % MgO and g) shows glassy phase and EDX spectrum of (f)

Fig. 11. Slice images of xyz planes for eight sequential slices of porous silicon nitride containing 12 % MgO (green region shows the solid body and black areas are pores)

Fig. 12. 3D reconstruction images of porous silicon nitride ceramic (orange region shows the solid body)

Fig. 13. Linear shrinkage and weight loss vs MgO content for samples heat-treated at 1700°C

Fig. 14. Porosity and density variation vs MgO content after heat-treatment at 1700°C

Fig. 15. Compression strength of samples vs MgO content heat-treated at 1700ºC

Table 1. Chemical compositions of the starting silicon

Element	Si	C	O	Fe	Al	Ca
Value (%)	100.000	<0.1	1.3	0.001	<0.001	0.0003

Table 2. Phase fractions and α/β-Si_3N_4 phase ratio obtained by XRD from samples containing different MgO contents and nitrided at 1425ºC

MgO content	**wt. %**			
	α-Si_3N_4	**β-Si_3N_4**	**α/β-Si_3N_4**	**Si_2N_2O**
0 % MgO	30.8	69.2	0.4	0
3 % MgO	60.4	34.7	1.7	4.9
6 % MgO	56.5	34.2	1.6	9.3
9 % MgO	51.8	35.4	1.4	12.8
12 % MgO	51.6	33.6	1.5	14.8

Table 3. Phase fractions and α/β-Si_3N_4 phase ratio obtained for samples containing 12 % MgO and heat-treated at different temperatures

Heat-treatment temperature	**wt. %**						
	Si	**MgO**	**Mg_2SiO_4**	**Si_2N_2O**	**α-Si_3N_4**	**β-Si_3N_4**	**α/β-Si_3N_4**
T=525℃	97.5	2.5	0	0	0	0	0
T=1100℃	95	2	3	0	0	0	0
T=1200℃	91.0	0	9	0	0	0	0
T=1300℃	94.0	0	4.0	2.0	0	0	0
T=1350℃	90.5	0	4.0	2.5	2.3	0.6	3.8
T=1400℃	49.4	0	1.5	7.4	29.2	12.5	2.3
T=1425℃	0	0	0	14.8	51.6	33.6	1.5
T=1700℃	0	0	0	0	0	100	0

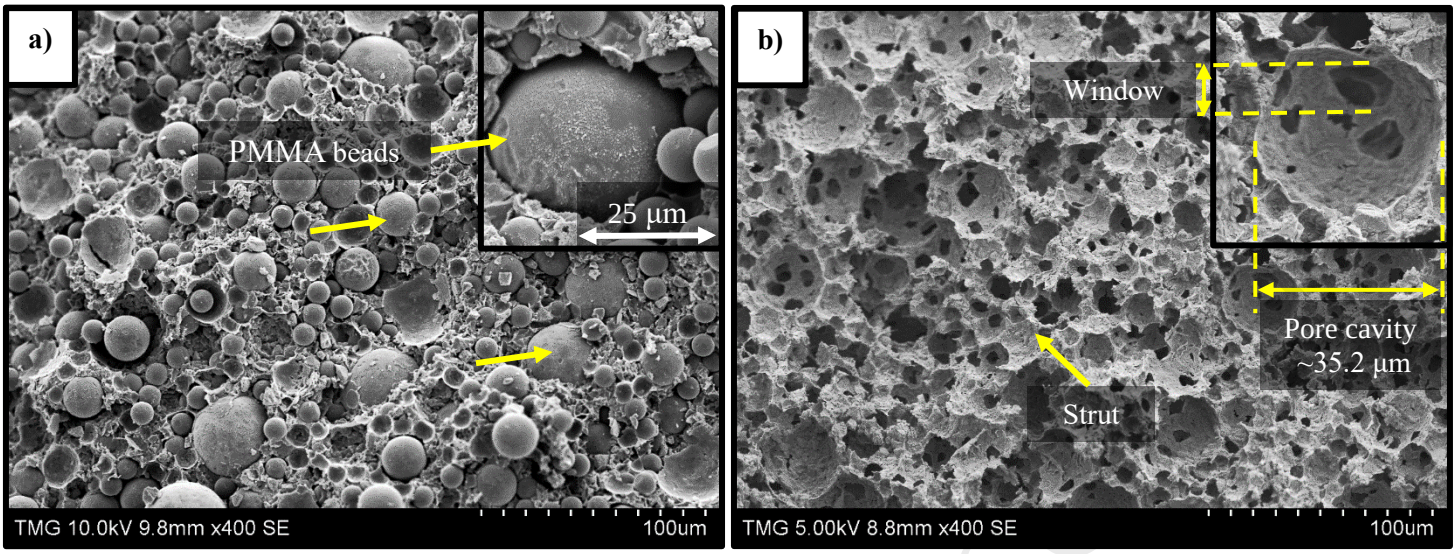

Fig. 1. SEM micrographs of a) as dried precursor containing polymer beads and b) after pyrolysis

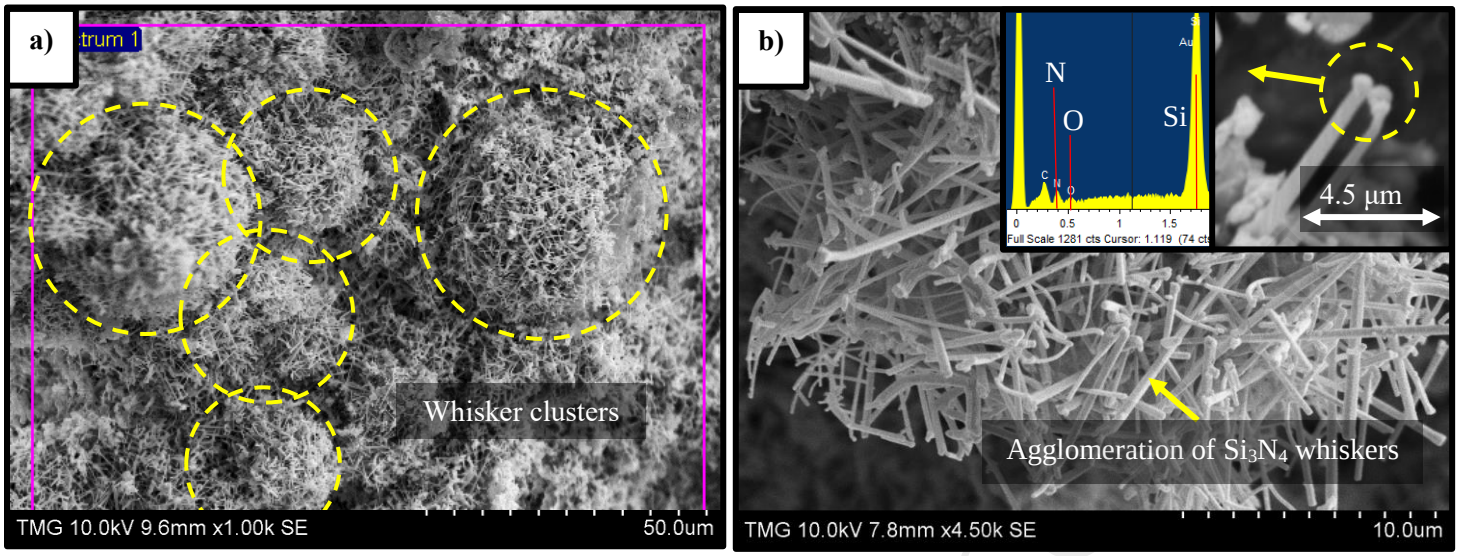

Fig. 2. SEM of fracture surface at two different magnifications illustrating the blocked pores with silicon nitride whiskers

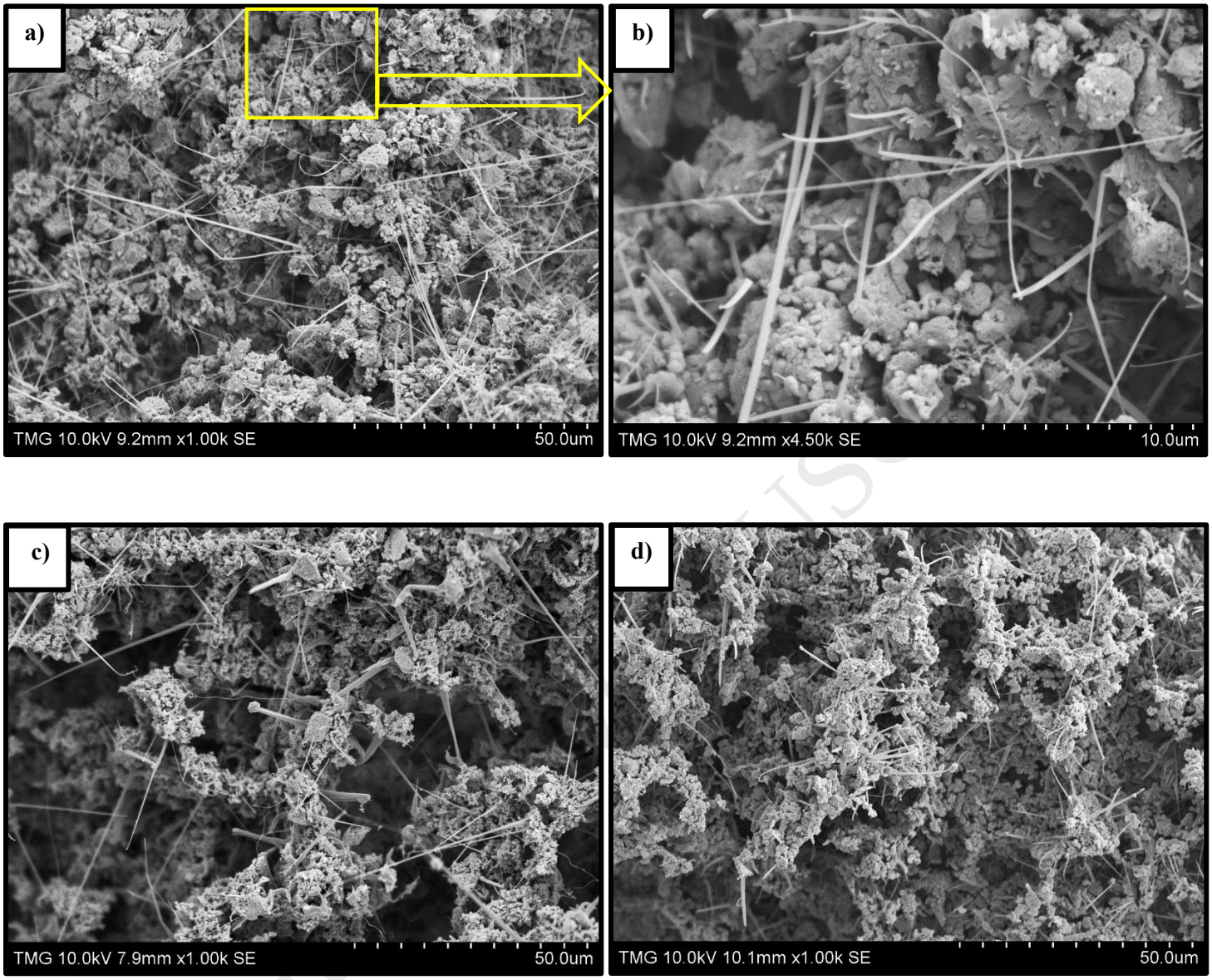

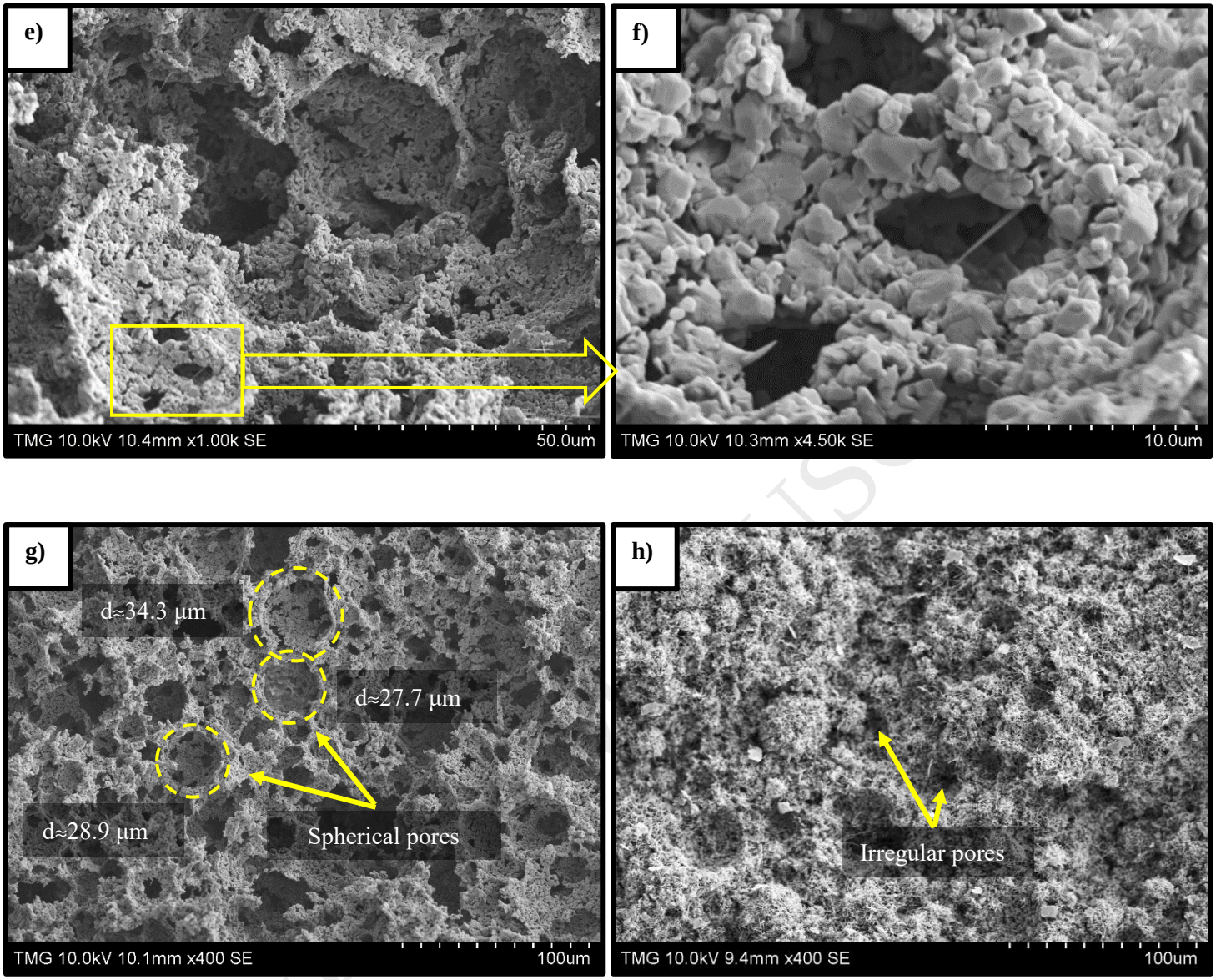

Fig. 3. SEM of fracture surfaces illustrating the pore structures in the presence of different MgO contents nitrided at 1425ºC; a and b) 3 % MgO, c) 6 % MgO, d) 9 % MgO, and e, f and g) 12 % MgO, and compared to h) 0 % MgO

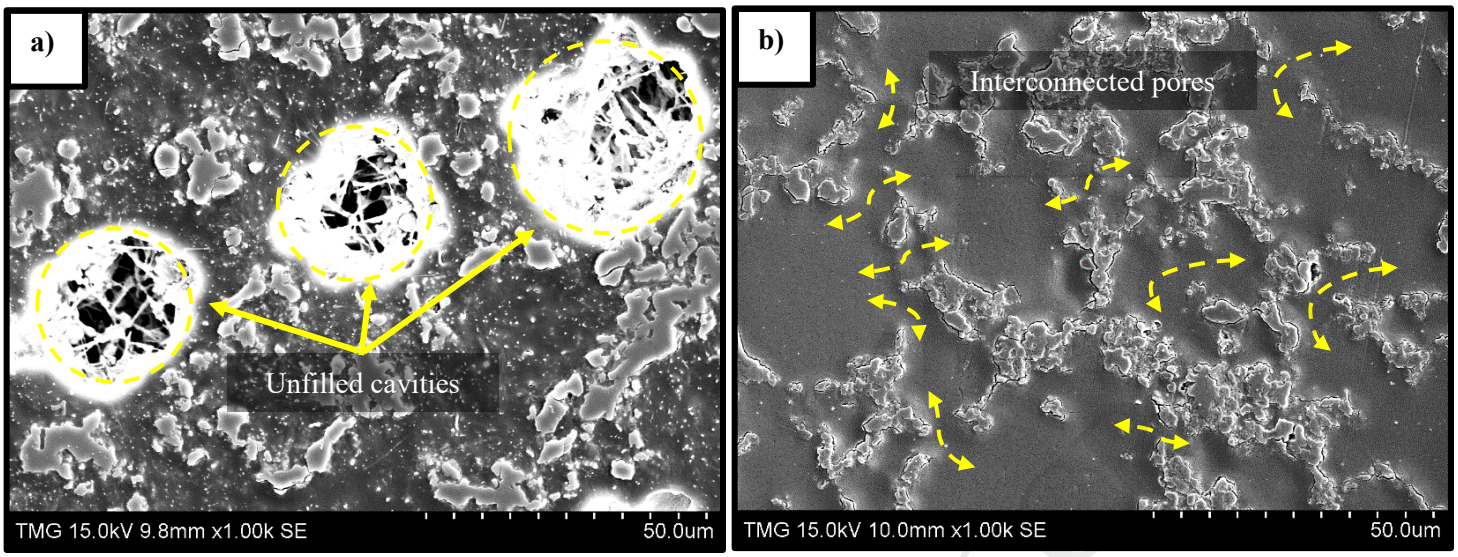

Fig. 4. Polished resin-infiltrated cross-sections showing the pore structures in silicon nitride containing a) 0 % MgO and b) 12 % MgO

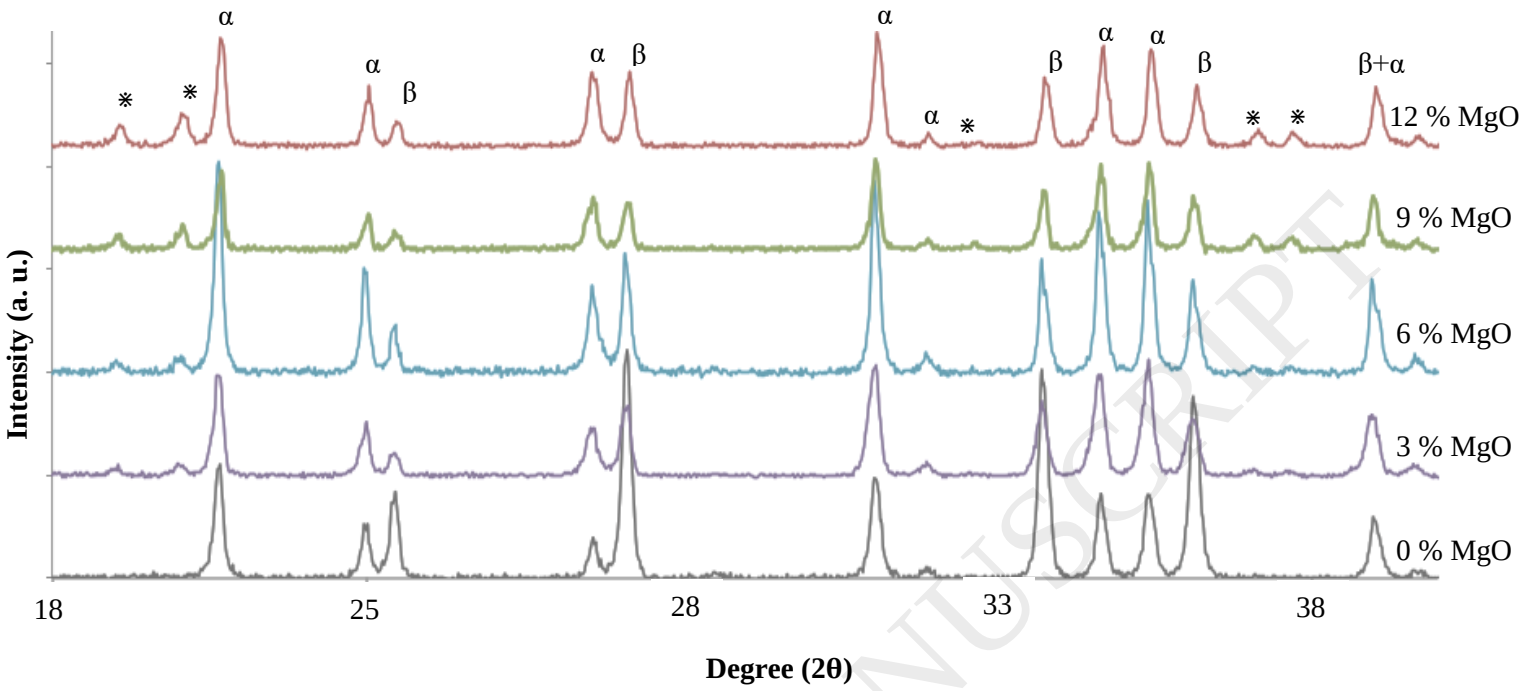

Fig. 5. XRD patterns of material nitrided at 1425°C with 0, 3, 6, 9 and 12 % MgO (α, β and ∗ show peaks corresponding to α-Si_3N_4, β-Si_3N_4 and Si_2N_2O, respectively)

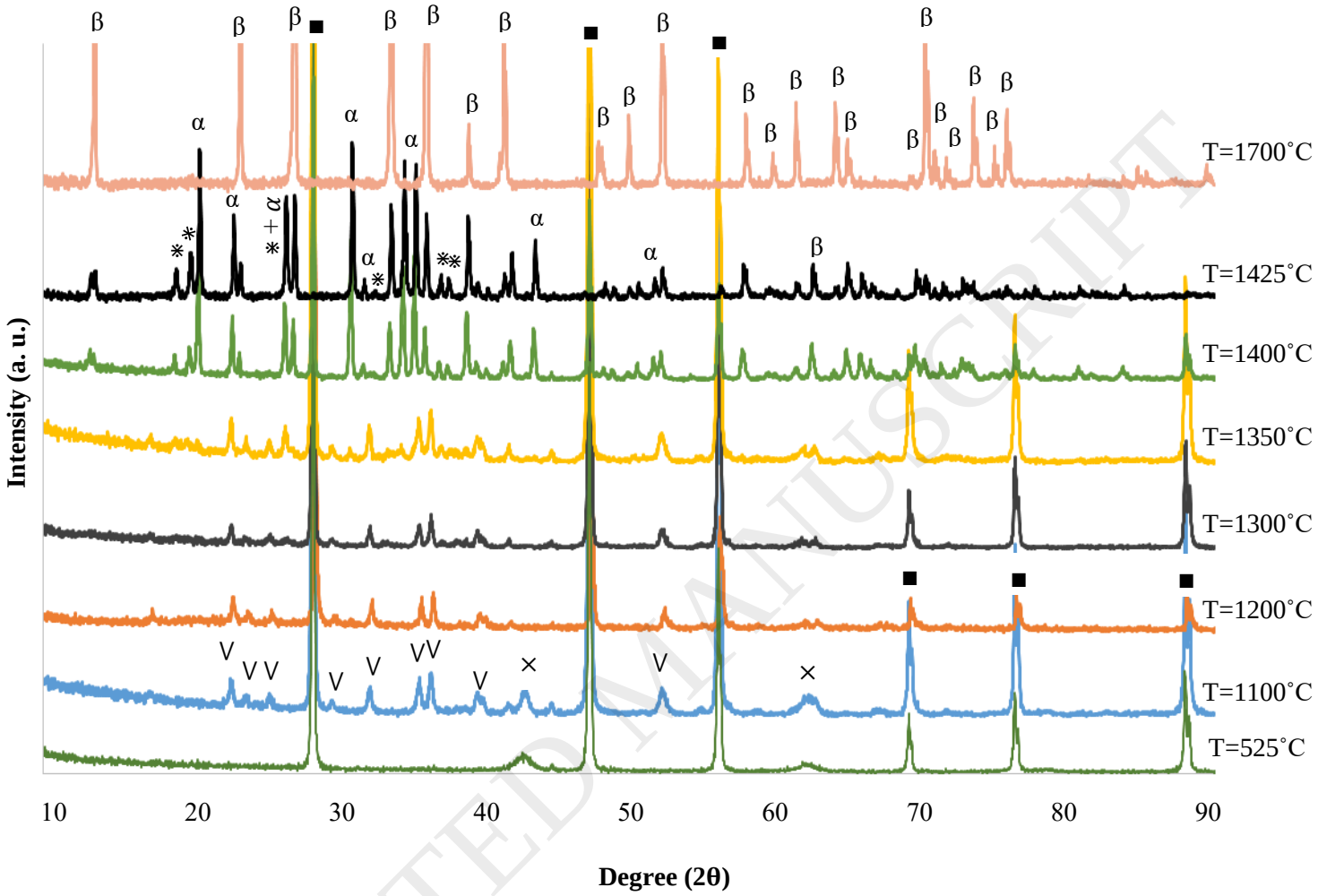

Fig. 6. XRD patterns of samples containing 12 % MgO heat-treated at 525, 1100, 1200, 1300, 1350, 1400, 1425 and 1700℃ (α, β , ∗, ∨, × and ■ show peaks corresponded to α-Si_3N_4, β-Si_3N_4, Si_2N_2O, Mg_2SiO_4, MgO and Si, respectively)

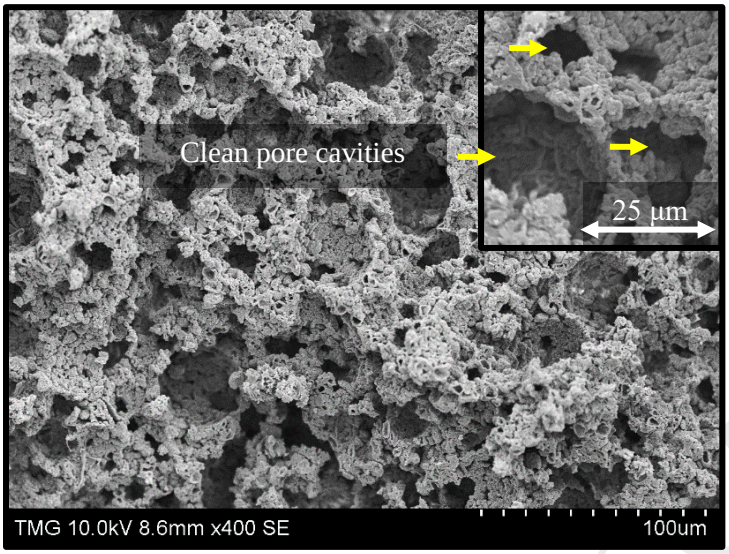

Fig. 7. SEM micrograph of pure silicon precursor nitrided on top of MgO powder bed

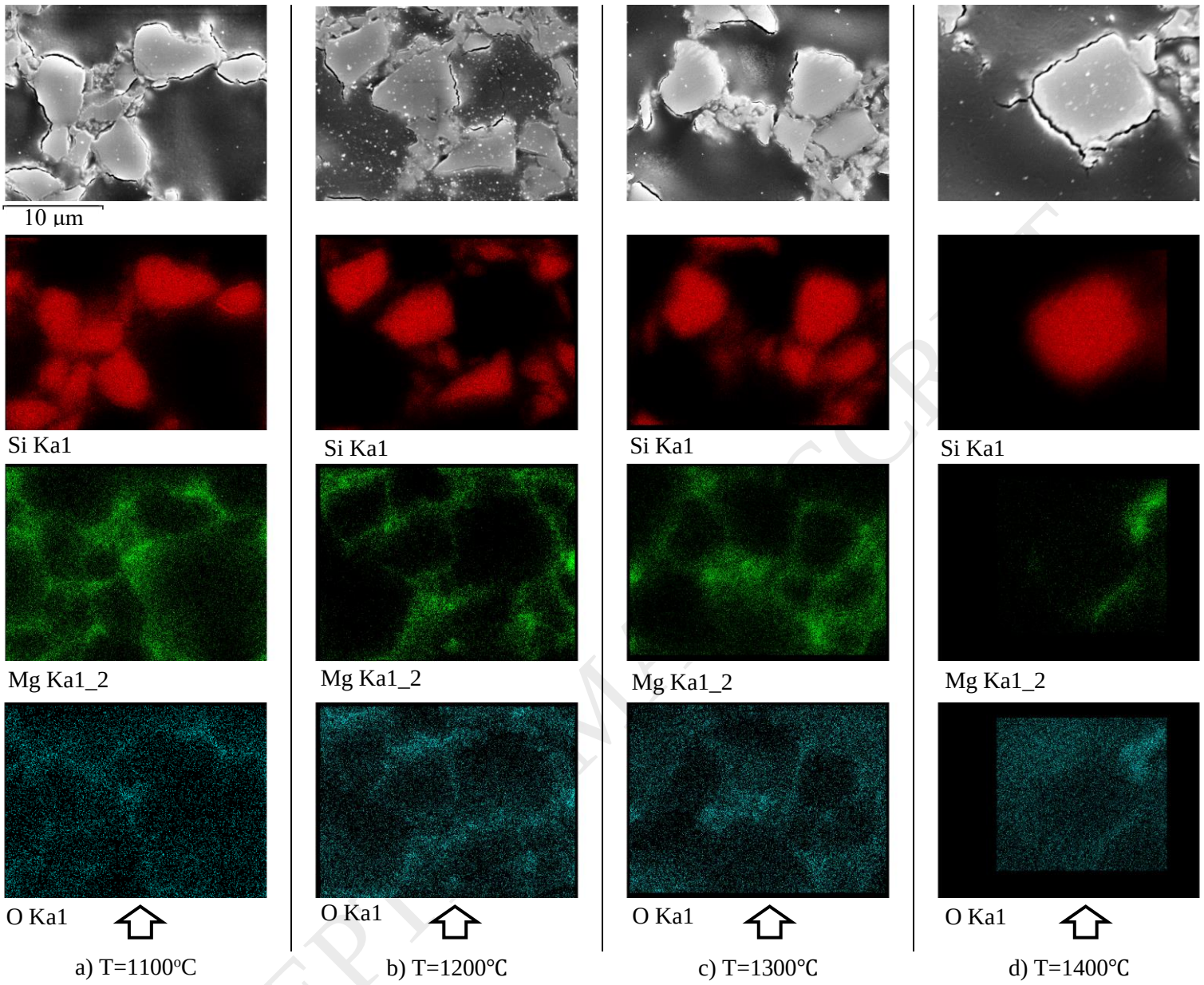

Fig. 8. EDX mapping of 12 % MgO addition to the porous silicon precursor and nitrided at different temperatures (note Mg and O segregation on the particle surfaces)

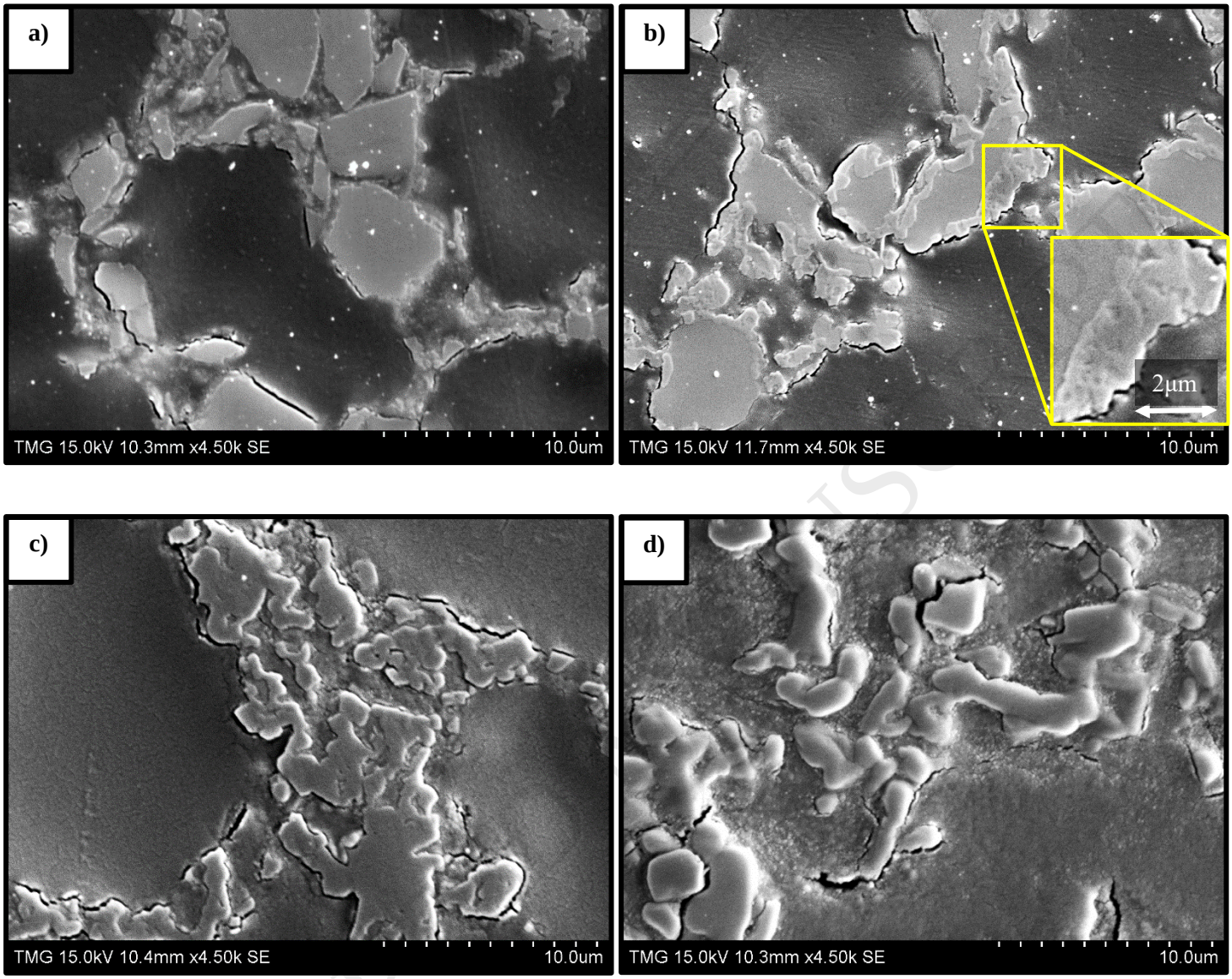

Fig. 9. Microstructural development and grain growth of the Si precursor containing 12 % MgO after heat-treatment at different temperatures: a) 1100℃, b) 1400℃, c) 1425℃ and d) 1700℃

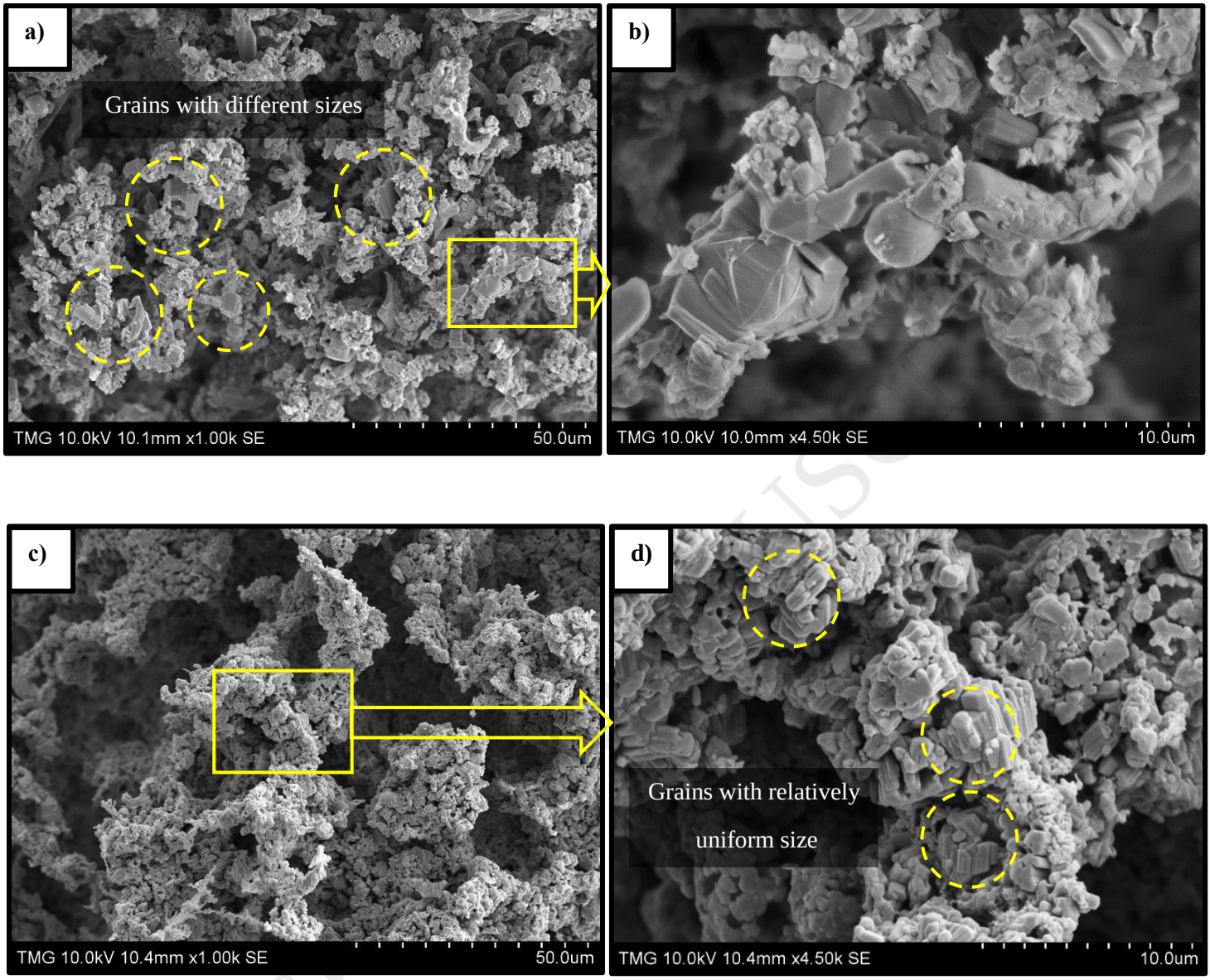

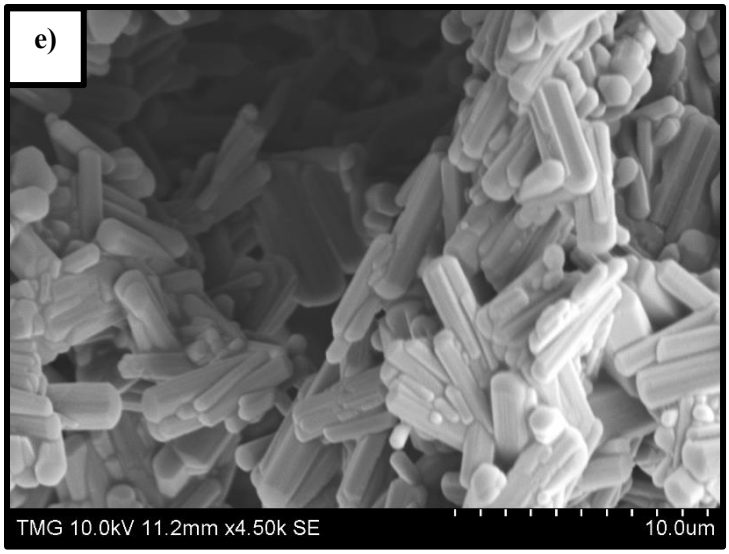

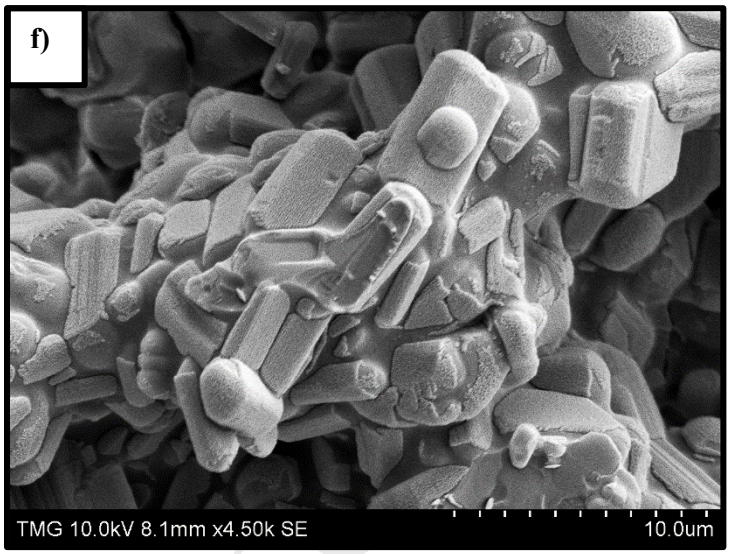

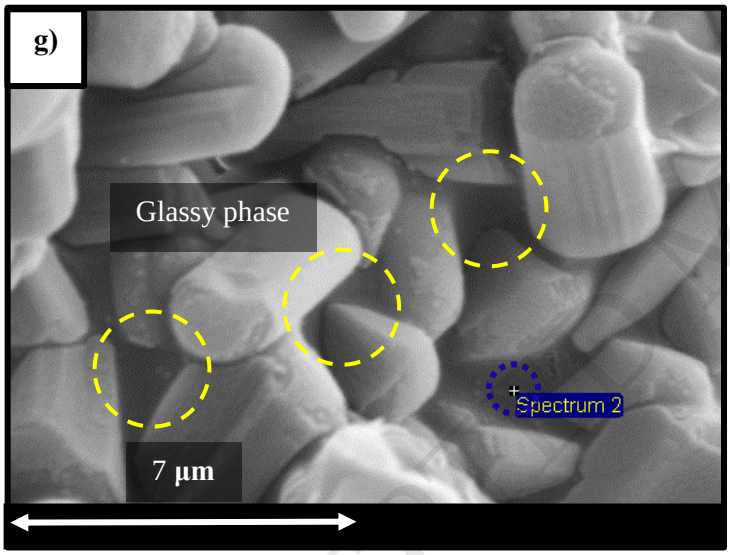

El.	N	O	Mg	Si	Total
wt. %	12.62	6.01	6.60	74.78	100.0
at. %	21.40	8.92	6.45	63.24	100.0

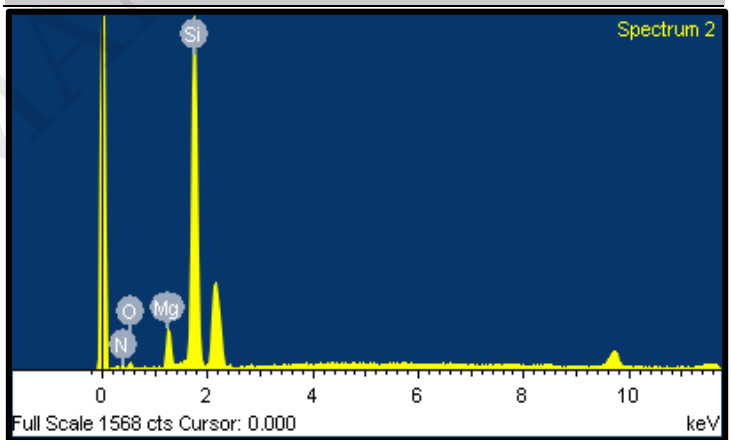

Fig. 10. SEM micrographs of various MgO precursor contents heat-treated at 1700°C: a and b) 3 % MgO, c and d) 6 % MgO, e) 9 % MgO, f) 12 % MgO and g) shows glassy phase and EDX spectrum of (f)

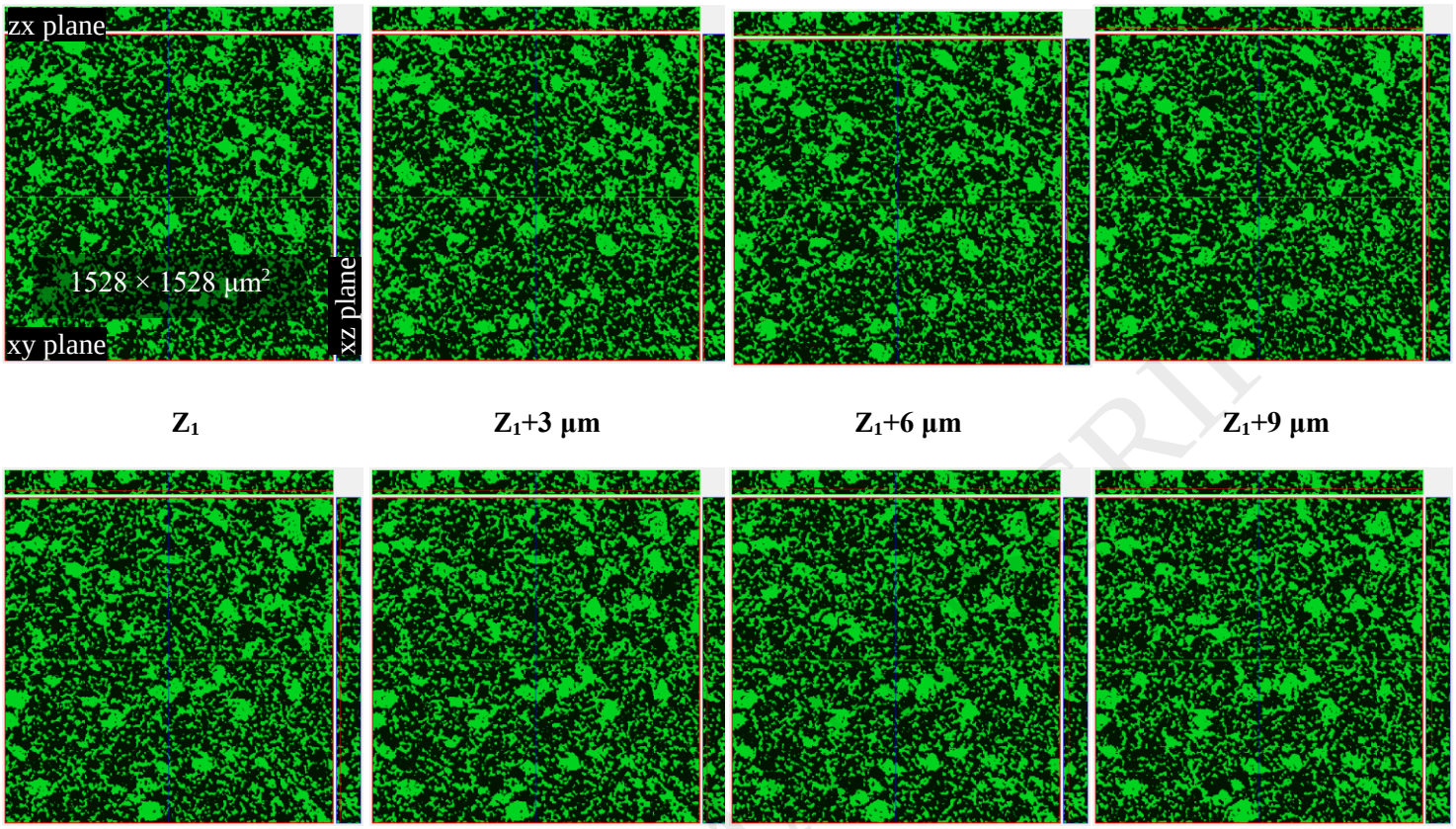

Fig. 11. Slice images of xyz planes for eight sequential slices of porous silicon nitride containing 12 % MgO (green region shows the solid body and black areas are pores)

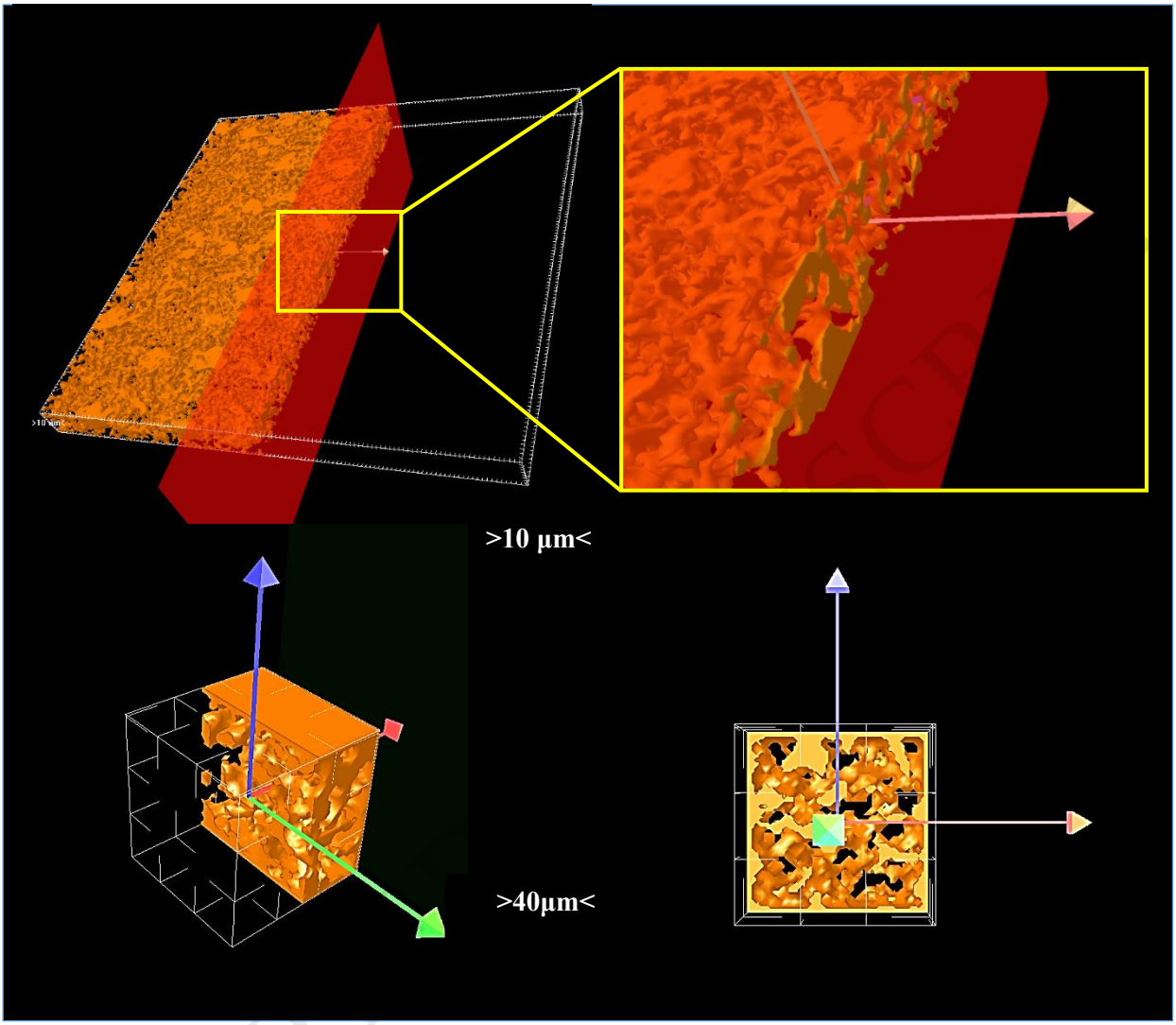

Fig. 12. 3D reconstruction images of porous silicon nitride ceramic (orange region shows the solid body)

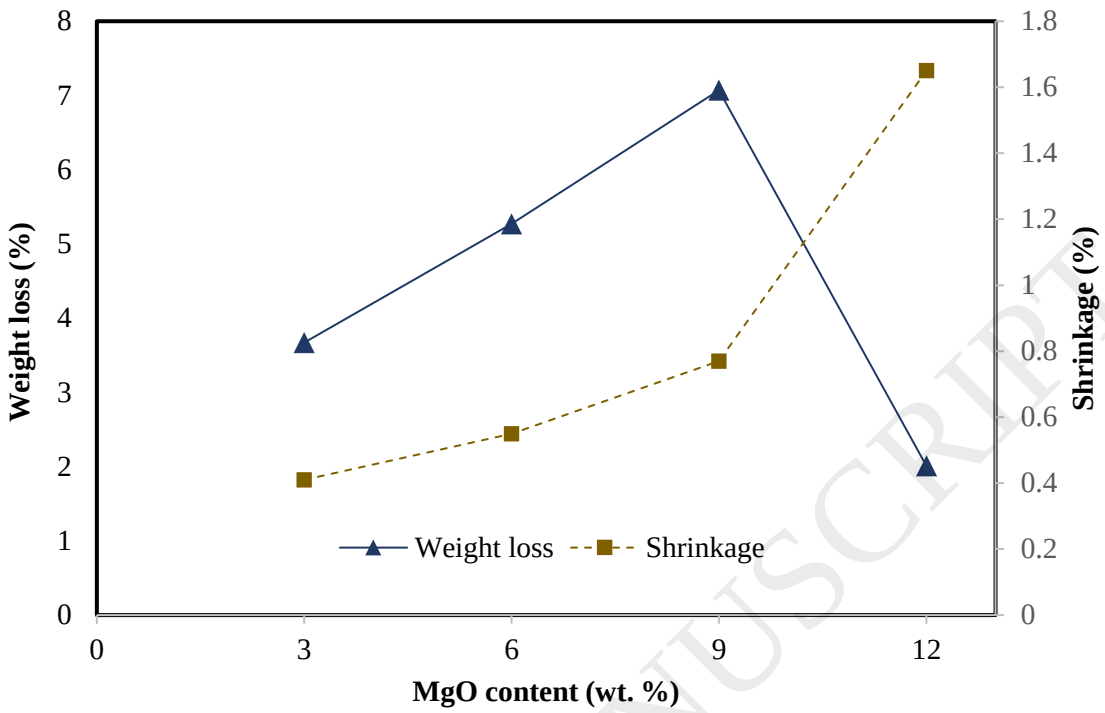

Fig. 13. Linear shrinkage and weight loss vs MgO content for samples heat-treated at 1700℃

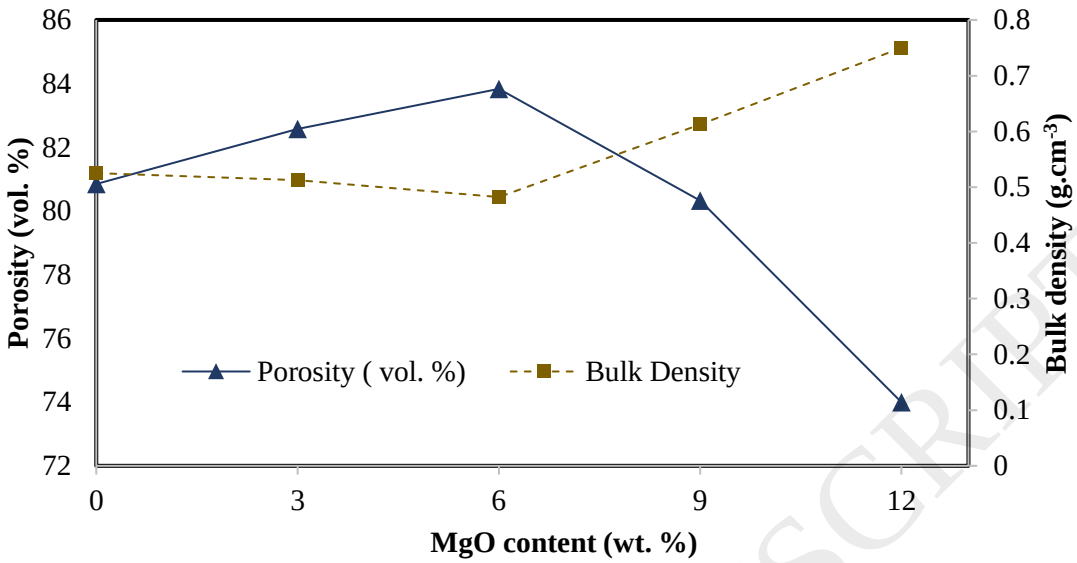

Fig. 14. Porosity and density variation vs MgO content after heat-treatment at 1700°C

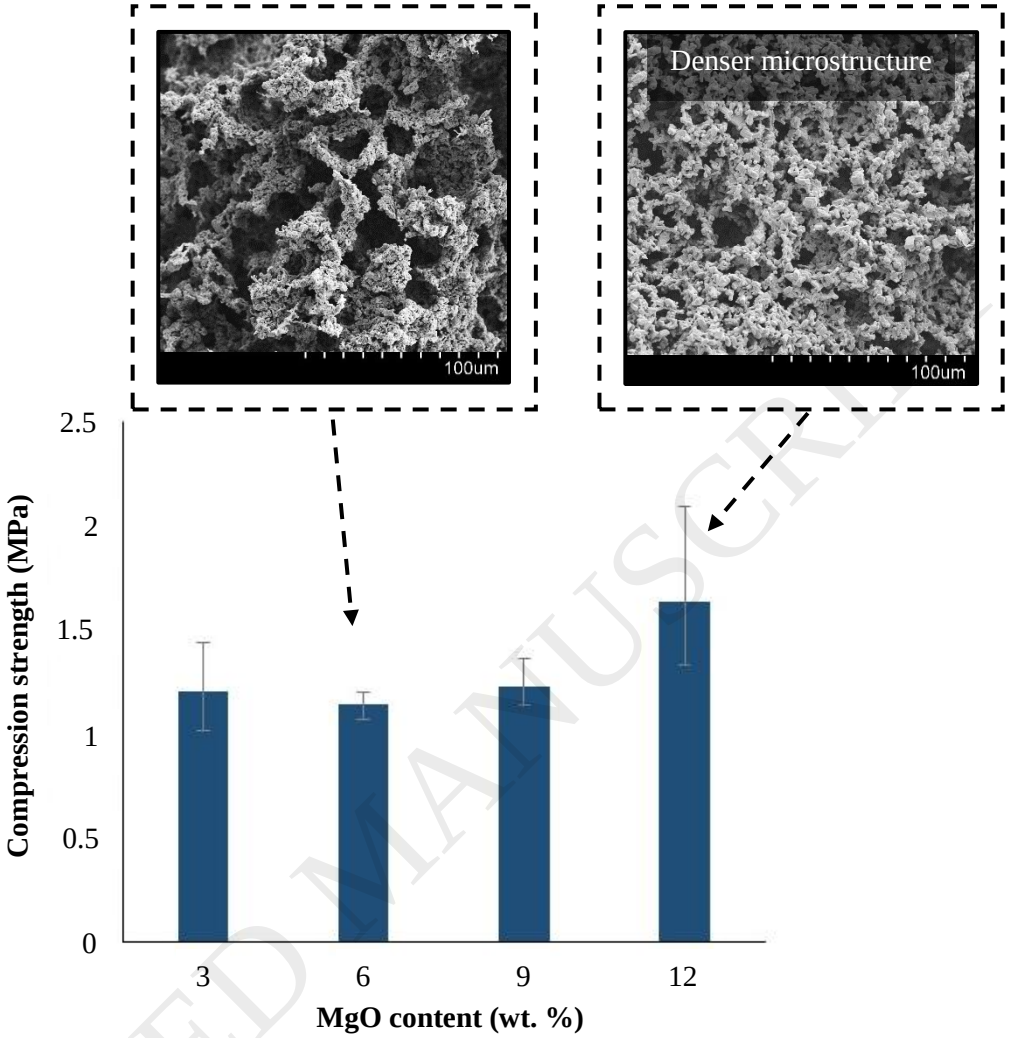

Fig. 15. Compression strength of samples vs MgO content heat-treated at 1700ºC